Modulational instability of geodesic-acoustic-mode packets

D. Korger [1,2,†], **E. Poli** [1], **A. Biancalani** [3], **A. Bottino** [1], **O. Maj** [1] and **J.N. Sama** [4]

[1]Max Planck Institute for Plasma Physik, D-85748 Garching, Germany

[2]Ulm University, D-89081 Ulm, Germany

[3]Léonard de Vinci Pôle Universitaire, Research Center, F-92916 Paris La Défense, France

[4]Institut Jean Lamour UMR 7198, Université de Lorraine-CNRS, F-54011 Nancy, France

Isolated, undamped geodesic-acoustic-mode (GAM) packets have been demonstrated to obey a (focusing) nonlinear Schrödinger equation (NLSE) (E. Poli, *Phys. Plasmas*, 2021). This equation predicts susceptibility of GAM packets to the modulational instability (MI). The necessary conditions for this instability are analysed analytically and numerically using the NLSE model. The predictions of the NLSE are compared with gyrokinetic simulations performed with the global particle-in-cell code ORB5, where GAM packets are created from initial perturbations of the axisymmetric radial electric field E_r. An instability of the GAM packets with respect to modulations is observed both in cases in which an initial perturbation is imposed and when the instability develops spontaneously. However, significant differences in the dynamics of the small scales are discerned between the NLSE and gyrokinetic simulations. These discrepancies are mainly due to the radial dependence of the strength of the nonlinear term, which we do not retain in the solution of the NLSE, and to the damping of higher radial spectral components k_r. The damping of the high-k_r components, which develop as a consequence of the nonlinearity, can be understood in terms of Landau damping. The influence of the ion Larmor radius ρ_i as well as the perturbation wavevector k_{pert} on this effect is studied. For the parameters considered here the aforementioned damping mechanism hinders the MI process significantly from developing to its full extent and is strong enough to stabilize some of the (according to the undamped NLSE model) unstable wavevectors.

Keywords: plasma simulation, plasma nonlinear phenomena, plasma confinement

---

1. Introduction

The geodesic acoustic mode (GAM) is a plasma oscillation observed in magnetic-confinement fusion reactors with toroidal geometry, such as tokamaks or stellarators (Winsor, Johnson & Dawson 1968). It develops because of the compressibility of the $E \times B$ drift velocity of the zonal flows (ZFs), where E and B denote the electric and magnetic field, respectively, which leads to ($m = \pm 1, n = 0$) pressure sidebands (where

† Email address for correspondence: david.korger@ipp.mpg.de

m and *n* are the poloidal and toroidal wavenumbers, respectively). As GAMs and ZFs satisfy charge neutrality, the perpendicular divergence of the diamagnetic current density is compensated by that of the polarization current, resulting in the GAM oscillation (Scott 2005; Qiu, Chen & Zonca 2018; Conway, Smolyakov & Ido 2021). The GAMs are thus recognized to be the non-stationary branch of the ZFs (Diamond *et al.* 2005; Conway *et al.* 2021) and their associated electric potential is (to the leading order) an $m = n = 0$ structure. The name GAM stems from the geodesic magnetic field line curvature, which is responsible for plasma compressibility and thus a necessary condition for the emergence of the characteristic pressure mode.

The interaction between GAMs and turbulence is fairly complex. Nonlinear self-interactions of drift-wave (DW) turbulence are one of the main mechanisms for generating the perturbations of the electric potential, which are the origin of ZFs and GAMs (Itoh *et al.* 2006). Meanwhile, similarly to the ZFs, GAMs are understood to suppress DW turbulence and regulate cross-field turbulence, thus enhancing energy confinement (Conway *et al.* 2021). Still, their direct effect on turbulence is not clear at the moment (Smolyakov *et al.* 2016), as GAMs are known to deplete the energy available to ZFs and transfer part of the energy of the system back to turbulence (Scott 2003*a*,*b*). This complex contribution to the turbulence dynamics makes GAMs highly interesting in current fusion research.

Prior studies have established that, as a direct consequence of nonlinear gyrokinetic theory, the GAM dynamics is well described by an equation of Schrödinger type – i.e. an equation whose linear contribution is exactly the linear Schrödinger equation, while the nonlinear dynamics necessitates an integro-differential expression, as has been discussed in § 6 of Qiu *et al.* (2018). Indeed, this is not surprising as it is a general result that plasma eigenmodes (more exactly, their radial envelope), arising in toroidal systems as a consequence of various types of instabilities, can be described by a nonlinear Schrödinger equation with integro-differential coefficients (Zonca & Chen 2014*a*,*b*; Zonca *et al.* 2015; Chen & Zonca 2016). For the reduced case of an isolated GAM (i.e. without interaction with other modes) a similar model equation is provided in Poli *et al.* (2021), where it was shown that, in the regime of moderate nonlinearity, the dynamics of undamped isolated GAM packets is well described by a cubic nonlinear Schrödinger equation (NLSE). The NLSE is a standard model (Spatschek 2012) for describing nonlinear dispersive oscillations with a (linear) dispersion relation of the form

$$\omega(k_r) = a + bk_r^2, \qquad \text{with arbitrary } a, b \in \mathbb{C}, \tag{1.1}$$

which, in the limit $k_r^2 \rho_i^2 \ll 1$ (where ρ_i denotes the ion Larmor radius and k_r is the radial wavevector associated with the GAM radial electric field), approximates to the standard gyrokinetic GAM dispersion relation (Smolyakov, Nguyen & Garbet 2008; Zonca & Chen 2008; Qiu, Chen & Zonca 2009), as will be discussed in § 2.1. The NLSE model has been applied and studied extensively in the contexts of deep water waves, light travelling through optical fibres, Bose–Einstein condensates and others (Kuznetsov, Rubenchik & Zakharov 1986; Agrawal 2019; Kengne, Liu & Malomed 2021). Some predictions of the NLSE are well known, like the emergence of solitons, nonlinear wave breaking, the nonlinear phase shift and susceptibility to the modulational instability (MI). While some of these phenomena have already been observed in gyrokinetic simulations of GAMs in Poli *et al.* (2021), thus confirming the NLSE as a valid description of the dynamics, in this report the focus is set on the MI, which to the best of the authors' knowledge has not yet been studied in the context of GAMs.

The MI is usually analysed for wave envelopes which consist of a (nearly) constant phase front that is modulated by a sinusoidal perturbation with a wavelength $\lambda_{\text{pert}} =$

$2\pi/k_{\mathrm{pert}}$. One finds that this perturbation is unstable under the conditions that the NLSE is self-focusing (which for GAMs is the case when the ratio τ_e between the electron temperature T_e and ion temperature T_i fulfills $\tau_e = T_e/T_i \lesssim 5.45$ Smolyakov *et al.* 2016) and the wavevector k_{pert} of the modulation of the envelope is within a certain range, which will be discussed in further detail in § 3. Unstable perturbations will grow exponentially at the expense of the constant envelope component until the sinusoidal modulation dominates the shape of the oscillation and saturates.

In the field of plasma physics the MI has been observed in numerous waves and oscillations (e.g. Schamel 1975; Murtaza & Salahuddin 1982). Most notable for the context of this paper are DWs, which as explained before are one of the driving mechanisms of GAMs and ZFs. The MI of DWs has been shown to spontaneously excite ZFs (Chen, Lin & White 2000) or increase their amplitude (Itoh *et al.* 2006). Since in this study the focus is set on isolated GAMs, where the effects of the generation mechanisms such as DWs are excluded, it is stressed here that in the present analysis the MI stems only from the self-interaction of GAMs and is not directly connected to DW MI.

After analysing the conditions for MI for the case of GAMs, the analytic predictions of the NLSE are first confirmed by numerical simulations of the NLSE and then validated against gyrokinetic simulations obtained from the global particle-in-cell code ORB5 (Bottino & Sonnendrücker 2015; Lanti *et al.* 2020). Details about the numerical tools are given in § 4. The results, which are presented in § 5, demonstrate that the MI does in fact appear in gyrokinetic GAM simulations, however, significant differences between the gyrokinetic and NLSE simulations are observed that can in part be explained by the (currently not included) radial dependency of the nonlinear strength $\alpha_{\mathrm{NL}} = \alpha_{\mathrm{NL}}(r)$ in the NLSE. Moreover, the radial spectra of the simulations indicate that a damping term should be included in the NLSE model in this context. The need to consider damping in the current context may at first seem surprising, since simulations are performed using a high safety factor ($q_s = 15$) and an initial k_r spectrum for which, according to theoretical predictions by Sugama & Watanabe (2006, 2007) and Qiu *et al.* (2009), it is expected that damping of GAMs is weak to negligible. However, the nonlinear evolution of the packet leads naturally to the generation of shorter and shorter wavelengths which are more efficiently damped. This effect is the nonlinear analogue of the enhanced Landau damping discussed in Palermo *et al.* (2016) and Biancalani *et al.* (2016), where the shorter wavelengths were generated by the linear dynamics in the presence of gradients.

In this paper, the theoretical predictions for the MI growth rate are modified with the inclusion of the damping rate derived in Qiu *et al.* (2009), which is appropriate in the in the underlying high safety factor q_s and high spectral wavevectors (high q_s, k_r) regime and is furthermore consistent with the approximation of adiabatic electrons employed in the gyrokinetic (GK) simulations. Good agreement between theory and GK simulations is found if the damping rate of Qiu *et al.* (2009) is multiplied by a factor of approximately 2.5 (see §§ 5.3 and 5.4). This is not unexpected, as a similar discrepancy has been already reported in previous benchmarks (Biancalani *et al.* 2017). The following § 5.5 includes these findings in the NLSE model and compares damped NLSE simulations with the GK results, which are observed to show good agreement.

Sections 5.6 and 5.7 illustrate the self-focusing of a GAM with unperturbed Gaussian initial condition, which is a phenomenon closely related to the MI, and a long GAM simulation depicting breather behaviour (see e.g. Akhmediev & Korneev 1986; Dudley *et al.* 2009) of the GAM MI.

2. Nonlinear Schrödinger equation model

2.1. *Introduction*

The NLSE model (Poli *et al.* 2021) describes the dynamics of an isolated GAM packet via the complex wavefunction $\psi(r, t)$, where its real part

$$\text{Re}[\psi(r, t)] \equiv E_r(r, t), \tag{2.1}$$

represents the axisymmetric component of the GAM radial electric field $E_r(r, t)$. The function ψ obeys the cubic NLSE given by

$$\text{i}\frac{\partial \psi}{\partial t} = \mathcal{F}\psi - \frac{\partial}{\partial r}\left(\frac{\mathcal{G}}{2}\frac{\partial \psi}{\partial r}\right) - \alpha_{\text{NL}}|\psi|^2\psi, \tag{2.2}$$

where the first two terms on the right-hand side characterize the linear GAM dispersion, while the last term introduces the contribution from nonlinear self-interactions. Their respective strengths are determined by the parameters $\mathcal{F}$, $\mathcal{G}$ and α_{NL}, which in most sections of this study will be assumed to be real values and independent of the radial coordinate r, which is equivalent to assuming no damping and a uniform plasma background, respectively. Damping in the NLSE will be considered later in this paper in §§ 5.2 and 5.5, and thus is discussed separately there.

The values of the parameters $\mathcal{F}$ and $\mathcal{G}$ are obtained from the analytical GK result for the linear GAM dispersion relation, which according to Smolyakov *et al.* (2016) is given by

$$\omega(k_r) = \omega_0\sqrt{1 + \tfrac{1}{2}k_r^2\rho_i^2 D(\tau_e)}, \tag{2.3}$$

and holds only when $k_r^2\rho_i^2 \ll 1$. Here, ω_0 is the dispersionless GAM frequency given by (2.5) below, k_r is the radial wavevector of the GAM spectrum, ρ_i is the ion Larmor radius and $D(\tau_e)$ is a coefficient characterizing the strength of the dispersive corrections, which depends on the electron-to-ion temperature ratio $\tau_e = T_e/T_i$

$$D(\tau_e) = \frac{3}{4} - \frac{\dfrac{13}{4} + 3\tau_e + \tau_e^2}{\dfrac{7}{4} + \tau_e} + \frac{\dfrac{747}{32} + \dfrac{481}{32}\tau_e + \dfrac{35}{8}\tau_e^2 + \dfrac{1}{2}\tau_e^3}{\left(\dfrac{7}{4} + \tau_e\right)^2}. \tag{2.4}$$

For ω_0 the expression derived in Sugama & Watanabe (2006) is utilized and damping is neglected

$$\omega_0^2 = \left[1 + \frac{2(23 + 16\tau_e + 4\tau_e^2)}{q_s^2(7 + 4\tau_e)^2}\right]\left(\frac{7}{4} + \tau_e\right)\frac{v_{Ti}^2}{R_0^2}, \tag{2.5}$$

where $v_{Ti} = \sqrt{2T_i/m_i}$ is the thermal ion velocity, m_i the ion mass, R_0 the major tokamak radius and q_s the safety factor. In order to obtain expressions for the parameters $\mathcal{F}$ and $\mathcal{G}$, the square root in the dispersion relation (2.3) is expanded using the approximation $k_r^2\rho_i^2 \ll 1$ that was already assumed to hold during the derivation of the dispersion relation

$$\omega \approx \omega_0 + \tfrac{1}{4}k_r^2\rho_i^2\omega_0 D =: \mathcal{F} + \tfrac{1}{2}\mathcal{G}k_r^2, \tag{2.6}$$

$$\mathcal{F} := \omega_0, \tag{2.7}$$

$$\mathcal{G} := \tfrac{1}{2}\omega_0\rho_i^2 D. \tag{2.8}$$

Here, a definition is denoted by ':='. For the strength α_{NL} of the nonlinear self-interaction term there currently exists no analytical expression. As a consequence

in this study the values for α_{NL} are obtained through comparisons with GK GAM simulations, which were generated with the particle-in-cell code ORB5 (Bottino & Sonnendrücker 2015; Lanti *et al.* 2020). The results of these comparisons are presented in Appendix A and show that the parameter is positive, $\alpha_{NL} > 0$, increases with τ_e and depends approximately inversely on the ion Larmor radius, $\alpha_{NL} \propto 1/\rho_i$. Furthermore, α_{NL} increases when approaching the centre of the plasma cross-section $r = 0$. No significant impact of the safety factor q_s on α_{NL} was found.

2.2. *Dynamics*

This section gives a short introduction to the terms in the NLSE (2.2), that will be relevant for the MI. The first term on the right-hand side, $\mathcal{F}\psi$, is responsible for the coherent oscillation of the GAM at the dispersionless frequency $\mathcal{F} = \omega_0$. The corresponding dynamics can be split off of the wavefunction ψ through the following transformation:

$$\psi(r, t) = \hat{\psi}(r, t) e^{-i\mathcal{F}t}, \tag{2.9}$$

where $\hat{\psi}$ is the envelope of the GAM packet. This ansatz reduces the NLSE to the usually reported form

$$i\frac{\partial \hat{\psi}}{\partial t} = -\frac{\mathcal{G}}{2}\frac{\partial^2 \hat{\psi}}{\partial r^2} - \alpha_{NL}|\hat{\psi}|^2\hat{\psi}. \tag{2.10}$$

The second term on the right-hand side of (2.2), $-\mathcal{G}/2\partial_r^2\psi$ (for $\mathcal{G} \neq \mathcal{G}(r)$), gives the dispersive properties to the GAM dynamics. The nature of the dispersion is determined by the sign of the parameter $\mathcal{G}$, which, as can be deduced from (2.4)–(2.8), depends solely on the value of the electron-to-ion temperature ratio τ_e, with $\tau_e \approx 5.45$ marking the boundary between positive and negative values of $\mathcal{G}$ (Nguyen, Garbet & Smolyakov 2008). The corresponding regimes are labelled as follows:

$$\left.\begin{matrix} \text{Anomalous Dispersion} & \mathcal{G} > 0 & \tau_e \lesssim 5.45, \\ \text{No Dispersion} & \mathcal{G} = 0 & \tau_e \approx 5.45, \\ \text{Normal Dispersion} & \mathcal{G} < 0 & \tau_e \gtrsim 5.45. \end{matrix}\right\} \tag{2.11}$$

The full dependency of $\mathcal{G}$ on τ_e is depicted in figure 1. The different kinds of dynamics corresponding to the three dispersion regimes are illustrated through NLSE simulations (without the nonlinear term) with an initial Gaussian profile in figure 2. The dispersive term broadens the width of packets as time progresses and alters the oscillation frequency of the Gaussian flanks compared with the maximum at $r = 0.5$ (a.u.), resulting in a curvature of the phase front in (r, t)-space. In the case of normal dispersion, the flanks oscillate faster than the packet centre, leading to convex curvature, and vice versa for anomalous dispersion.

The nonlinear term introduces a shift that lowers the frequency (due to $\alpha_{NL} > 0$ for GAMs) proportionally to the packet amplitude squared at the location r, which for $\mathcal{G} = 0$ amounts to

$$\Delta\omega_{NL}(r, t) = -\alpha_{NL}|\psi|^2(r, t). \tag{2.12}$$

This shift is illustrated in figure 3. The interaction between the nonlinear phase shift and the dispersive term creates two distinct regimes called self-defocusing regime (when $\mathcal{G}/\alpha_{NL} < 0$, i.e. for GAMs for normal dispersion, i.e. $\tau_e \gtrsim 5.45$) and self-focusing regime (for $\mathcal{G}/\alpha_{NL} > 0$, i.e. vice versa) (Scott 2006). Since the self-focusing regime is deeply
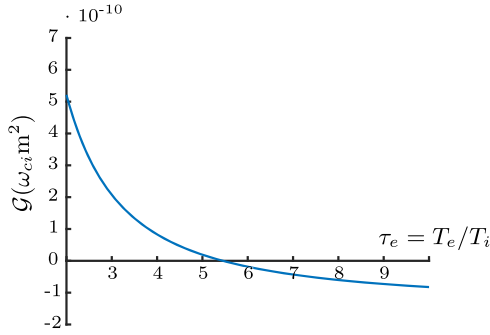
FIGURE 1. Dependency of the dispersion coefficient $\mathcal{G}$ on the electron-to-ion temperature ratio τ_e as defined in (2.4)–(2.8). The parameters were chosen as specified in table 1, with ion cyclotron frequency $\omega_{ci} \approx 1.82 \times 10^8$ (rad/s^{-1}) and ion Larmor radius $\rho_i/a_{\min} = 4.08 \times 10^{-4}$.
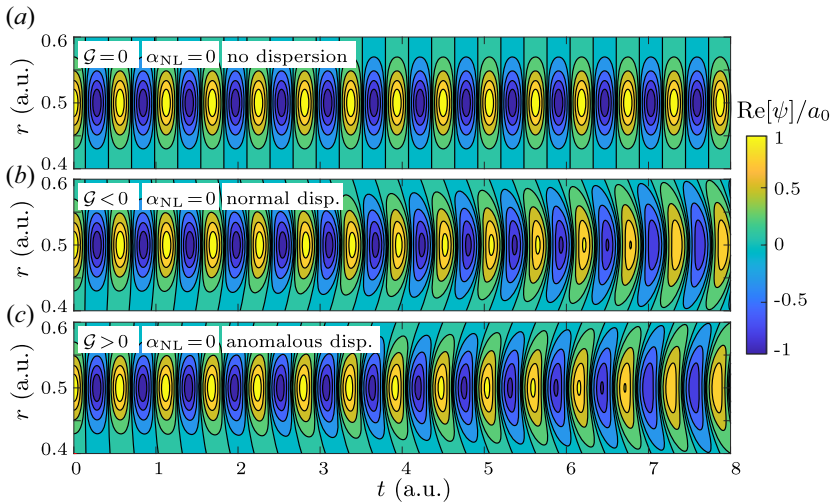

FIGURE 2. NLSE simulations illustrating the isolated impact of the dispersive term on the dynamics. The figure shows the real part Re[ψ] of the wavefunction (which for the GAM corresponds to the radial electric field E_r) normalized to the maximum amplitude a_0 of the Gaussian initial condition. The nonlinear term is disregarded ($\alpha_{NL} = 0$). The selected values of $\mathcal{F}$ and $\mathcal{G}$ are chosen such that their relative orders of magnitude match the GAM simulations considered in the later sections. It can be observed that the coefficient $\mathcal{F}$ is responsible for the oscillation of Re[ψ], while the dispersive term introduces a curvature in (r, t)-space as well as an increase of the Gaussian width as time progresses.

connected with the formation of MI, it will be explained in further detail in the next section.

3. Modulational instability

We recall in this section some known results concerning the MI. Although the material reported here can be found in textbooks (e.g. Agrawal 2019), we present it to put the results of the next sections into context. The MI, also called Benjamin–Feir instability (Benjamin & Feir 1967), is believed to be one of the most ubiquitous instabilities in nature (Zakharov & Ostrovsky 2009). It appears not only in the NLSE, but also in other equations describing
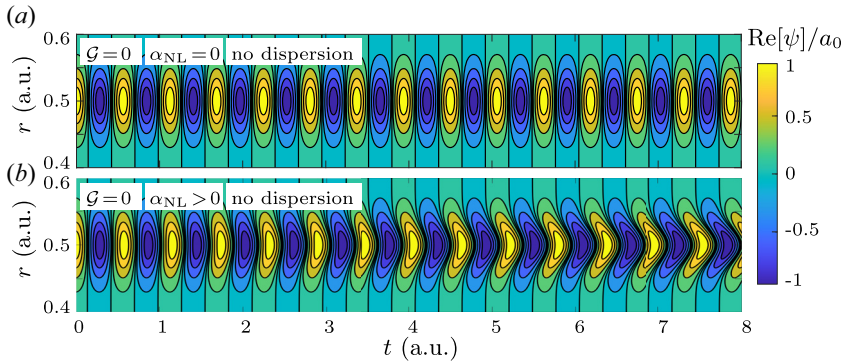
FIGURE 3. NLSE simulations illustrating the nonlinear frequency shift (in the dispersionless regime, $\mathcal{G} = 0$) for a Gaussian initial condition. Similarly to figure 2 the real part $\mathrm{Re}[\psi]$ of the wavefunction is illustrated, which corresponds to the GAM radial electric field E_r. Comparing the upper simulation (without nonlinearity, $\alpha_{\mathrm{NL}} = 0$) with the lower one, it is evident to see that the frequency shift as described by (2.12) is most pronounced at the centre of the Gaussian at $r = 0.5$, since there the amplitude reaches its highest value.

nonlinear dispersive waves, e.g. in the Withham equation and the Korteweg–de Vries equation. The instability only develops when the nonlinear and dispersive contributions to the oscillation dynamics interact such that the NLSE is self-focusing. As the name suggests, the NLSE dynamics creates a self-focusing effect of maxima in the wave packet, which is explained in further detail in Appendix B.

3.1. *Introduction and behaviour*

The MI is usually analysed for the case of a plane wave $A_0(t)$ with amplitude a_0 (which can be considered to be a packet with very large width, $k_r \rightarrow 0$) superimposed with a radially periodic perturbation A_1 with a wavevector k_{pert}

$$\psi(r, t) = [A_0(t) + A_1(r, t)] \exp(-\mathrm{i}\omega_0 t), \tag{3.1}$$

$$A_1(r, t = 0) = a_1 \cos(k_{\mathrm{pert}} r), \quad a_1 \ll a_0. \tag{3.2}$$

When the perturbation wavevector k_{pert} lies in the unstable range, which will be specified in § 3.2, due to the previously mentioned self-focusing effect the sinusoidal perturbation will grow exponentially (as long as the perturbation amplitude a_1 is small compared with the plane wave amplitude a_0) at the expense of the plane wave ($k_r = 0$) component of the wave, which in the following will be called the background wave. More details on the growth process are given in Appendix B. When the perturbation has grown so large that it dominates the shape of the wave ψ it saturates and acquires a large nonlinear phase shift (as mentioned in § 2.2) compared to the background, leading to strongly incoherent phase fronts. In this saturation phase the radial spectrum of the wave contains many high-k_r components. When the nonlinear phase shift is large enough that the perturbation has skipped an entire oscillation compared with the background, the wave front reconnects and the perturbation decreases again. Finally, the initial condition is restored and the MI process can start anew, leading to a cyclic behaviour called Akhmediev breathers (Akhmediev & Korneev 1986). A single Akhmediev breather cycle together with the corresponding radial spectrum is shown in figure 4.

(*a*)   Re[ψ]/a₀

(*b*) |𝔉[Re[ψ]]| (a.u.)
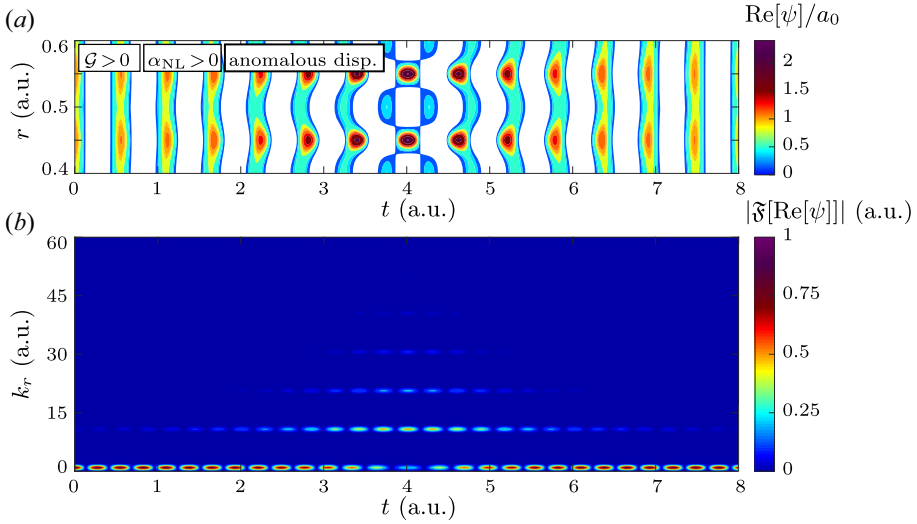

FIGURE 4. Single cycle of an Akhmediev breather where the initial perturbation wavevector was chosen to be $k_r = 10$ (a.u.). The upper figure illustrates $\mathrm{Re}[\psi]/a_0$, which for the GAM corresponds to the radial electric field E_r. As indicated by the colour bar only the positive values are drawn in the figure to emphasize the decoherent phase front at $t = 4$ (a.u.). The bottom figure shows the evolution of the corresponding radial spectrum (i.e. the absolute value of the Fourier transform $|\mathfrak{F}[\mathrm{Re}[\psi]]|$). The perturbation grows exponentially until $t \approx 2.5$, after which the growth slows down and at $t \approx 4$ the perturbation reaches its maximum value (which can be seen in the spectrum as well as in real space).

3.2. *Conditions for instability*

The conditions for instability will be briefly summarized in the following (see e.g. Remoissenet 1996). By assuming that the time evolution of the perturbation $A_1(r, t)$ will be of the form

$$A_1(r, t) = \frac{a_1}{2} \exp(i(k_{\mathrm{pert}}r - \omega_{\mathrm{pert}}t)) + \frac{a_1^*}{2} \exp(-i(k_{\mathrm{pert}}r - \omega_{\mathrm{pert}}t)), \qquad (3.3)$$

one finds that ω_{pert} fulfils the dispersion relation

$$\omega_{\mathrm{pert}}^2 = \left(k_{\mathrm{pert}}^2 - 4\frac{\alpha_{\mathrm{NL}}}{\mathcal{G}}a_0^2 \right) \frac{\mathcal{G}^2 k_{\mathrm{pert}}^2}{4}. \qquad (3.4)$$

It is immediate to see that exponential growth occurs (i.e. ω_{pert} is imaginary) when firstly

$$\frac{\alpha_{\mathrm{NL}}}{\mathcal{G}} > 0, \quad (\Leftrightarrow \text{NLSE is self-focusing}), \qquad (3.5)$$

which due to $\alpha_{\mathrm{NL}} > 0$ for GAMs is equivalent to requiring anomalous dispersion ($\mathcal{G} > 0$, $\tau_e \lesssim 5.45$ as described in § 2.2), and secondly when the perturbation wavevector is within the range

$$|k_{\mathrm{pert}}| < |k_{\mathrm{lim}}| = 2a_0\sqrt{\frac{\alpha_{\mathrm{NL}}}{\mathcal{G}}} = \sqrt{2}k_{\mathrm{max}}, \qquad (3.6)$$

where k_{lim} marks the boundary between stable and unstable perturbation wavevectors. The perturbation wavevector k_{pert}^2 provides the frequency mismatch of the sideband wave with
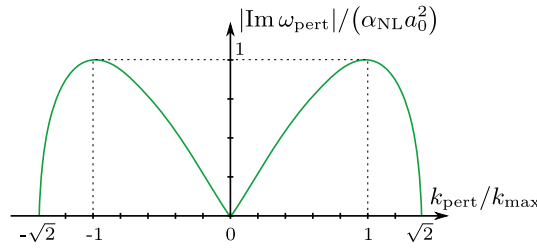
FIGURE 5. Dependency of the MI growth rate $\gamma_{MI} := |\operatorname{Im} \omega_{pert}|$ on the perturbation wavenumber k_{pert}, as given by (3.7). It is assumed that the first condition, given by (3.5), is satisfied, i.e. dispersion is anomalous.

respect to the background (pump) wave. The corresponding growth rate, which will be labelled $\gamma_{MI} := |\operatorname{Im} \omega_{pert}|$ in the following, reaches its maximum value at the wavevector $|k_{max}| := a_0 \sqrt{2\alpha_{NL}/\mathcal{G}}$. From (3.4) one finds that

$$\gamma_{MI}(k_{pert}) = \left| \operatorname{Im} \left[\frac{\mathcal{G} k_{pert}}{2} \sqrt{k_{pert}^2 - 4\frac{\alpha_{NL}}{\mathcal{G}} a_0^2} \right] \right|, \tag{3.7}$$

$$\gamma_{MI}(k_{pert} = k_{max}) = \alpha_{NL} a_0^2. \tag{3.8}$$

The full dependency of γ_{MI} on the wavevector of the initial perturbation k_{pert} is illustrated in figure 5.

4. Numerical approach

This section introduces the numerical tools employed in this paper to simulate the GAM gyrokinetically and with the NLSE model. As mentioned in the introduction, § 1, the GK results, which are obtained using the global particle-in-cell code ORB5 (Bottino & Sonnendrücker 2015; Lanti *et al.* 2020), are assumed to provide an accurate physical description of the GAM dynamics and are thus an adequate reference solution to validate the NLSE results and show shortcomings of this simplified model.

4.1. *Split-step NLSE solver*

The split-step solver (SSS) code was written by G.P. Agrawal (Agrawal 2019) in MatLab and was created to solve the NLSE (2.10), which describes the dynamics of the envelope, in the context of optical fibres where it is reported. The code was modified to incorporate the originally missing oscillation term by utilizing the transformation introduced in (2.9) and adapted to make its input and output consistent with ORB5 simulations.

The split-step method states that, if the chosen numerical time step Δt is small enough, the nonlinear and dispersive contributions to the NLSE dynamics (of the wave envelope $\hat{\psi}$) act (mostly) independently from each other (Faou 2012; Agrawal 2019). It follows that the solution can be approximated by alternatingly solving the two equations

$$i\frac{\partial \hat{\psi}}{\partial t} = -\alpha_{NL}|\hat{\psi}|^2\hat{\psi} \quad \text{(isolated nonlinear dynamics)}, \tag{4.1}$$

$$i\frac{\partial \hat{\psi}}{\partial t} = -\frac{\mathcal{G}}{2}\frac{\partial^2 \hat{\psi}}{\partial r^2}, \quad \text{(isolated dispersive dynamics)}, \tag{4.2}$$

for each time step. This approach has the significant advantage that the equations for the isolated nonlinear and isolated dispersive dynamics can each be immediately solved from

an initial condition $\hat{\psi}(r, t = 0) = \hat{\psi}_0$ using the following analytic solutions:

$$\hat{\psi}_{\text{NL}}(r, t) = \exp(\text{i}\alpha_{\text{NL}}|\hat{\psi}_0|^2 t)\hat{\psi}_0 =: \varphi_{\text{NL}}^t[\hat{\psi}_0], \tag{4.3}$$

$$\hat{\psi}_D(r, t) = \mathfrak{F}^{-1}\left\{\exp\left(-\text{i}t\frac{\mathcal{G}}{2}k^2\right)\mathfrak{F}\{\hat{\psi}_0\}\right\} =: \varphi_D^t[\hat{\psi}_0], \tag{4.4}$$

where $\mathfrak{F}\{\cdot\}$ is the spatial Fourier transform which is calculated using the fast-Fourier-transform algorithm, $\mathfrak{F}^{-1}\{\cdot\}$ denotes the inverse Fourier transform and $\varphi_{\text{NL}}^t[\cdot]$ and $\varphi_D^t[\cdot]$ denote the exact flows (i.e. the temporal evolution starting from an initial condition $\hat{\psi}_0(r)$) for the isolated nonlinear and isolated dispersive equation, respectively.

The flow φ_{NLSE}^t associated with the complete dynamics of the NLSE is then approximated as follows:

$$\hat{\psi}(r, t = n\Delta t) = \varphi_{\text{NLSE}}^{n\Delta t}[\hat{\psi}_0] \approx (\varphi_D^{\Delta t} \circ \varphi_{\text{NL}}^{\Delta t})^n[\hat{\psi}_0], \tag{4.5}$$

also known as the Lie splitting method, where '$\circ$' denotes the concatenation of flows, $(\varphi_D^{\Delta t} \circ \varphi_{\text{NL}}^{\Delta t})[\hat{\psi}_0] = \varphi_D^{\Delta t}[\varphi_{\text{NL}}^{\Delta t}[\hat{\psi}_0]]$.

The SSS implements a refinement of the split-step method with higher accuracy, called the symmetrized split-step Fourier method or Strang splitting scheme. In this form, the nonlinear dynamics is split into two parts of duration $\Delta t/2$, with the dispersive (and thus smoothing) evolution acting in between (Faou 2012; Agrawal 2019).

4.2. *ORB5*

The GK code ORB5 (Bottino & Sonnendrücker 2015; Lanti *et al.* 2020) is a global particle-in-cell code that simulates the plasma dynamics inside a tokamak for processes occurring on a time scale slower than that of the ion gyromotion. It can be executed with or without nonlinear plasma interactions.

The GK theory reduces the six-dimensional kinetic theory by one dimension by averaging over the gyromotion to obtain a five-dimensional problem describing the dynamics of the guiding centre distribution function f_s of each species s. The set of GK equations describing the dynamics of f_s can be constructed in different ways. The model implemented in ORB5 is derived from a GK Lagrangian describing the particle motion in a magnetic field (Brizard & Hahm 2007). The time-symmetric Hamiltonian within the Lagrangian conserves energy automatically, leading to a model which is particularly useful for numerical simulations (Bottino & Sonnendrücker 2015). ORB5 provides numerical results that exhibit strong agreement with other GK codes (Lanti *et al.* 2020). Its recent application to the dynamics of isolated GAMs is documented in Palermo *et al.* (2016), Biancalani *et al.* (2016), Palermo *et al.* (2017), Palermo, Poli & Bottino (2020), Poli *et al.* (2020) and Palermo *et al.* (2023). The interested reader is referred to these references for more details about the numerical model.

In order to create GAMs in the ORB5 simulations, an electric field E_r is initialized in ORB5 via a perturbation δn_i of the gyrocentre density of the only ion species included in the simulations. This perturbation leads through the GK Poisson equation to a potential perturbation (or equivalently to a polarization density) that ensures quasineutrality. The relevant relation between density perturbation and electric field for a $(0,0)$ perturbation can be expressed as

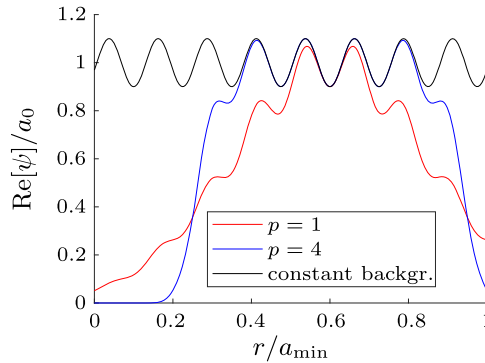$$\delta n_i(r) \propto \frac{1}{r}\frac{\partial}{\partial r}(rE_r(r)). \tag{4.6}$$

FIGURE 6. Initial condition of the GAM radial electric field $E_r = \mathrm{Re}[\psi]$ according to (5.1) for two values of p, compared with the usual constant background initial condition of MI described in §3.1. Unless stated otherwise, $p = 4$ will be used for the packet steepness, $w_0 = 0.35 a_{\min}$ for the width and the centre will be placed at $r_0 = 0.6 a_{\min}$ in subsequent simulations. The perturbation wavevector and amplitude in this example are $k_{\mathrm{pert}} = 8(2\pi/a_{\min})$ and $a_1 = 0.1$, respectively.

As a result, the GAM is essentially 'dropped into' the simulations and the formation process is not considered.

5. Simulation results

In the following simulations the (axisymmetric) GAM radial electric field is initialized in the following form:

$$E_r(r, t = 0) = a_0 \exp\left(-\left[\frac{r - r_0}{w_0}\right]^{2p}\right)\left(1 + a_1 \cos(k_{\mathrm{pert}}[r - r_0])\right), \qquad (5.1)$$

which is similar to the initial condition discussed in (3.1) in §3, but uses a plateau function instead of a constant background in order to avoid numerical artefacts at the boundaries of the simulation domain, i.e. $r = 0$ and $r = a_{\min}$. This initial condition is depicted for different parameters in figure 6. The exponent p determines the steepness of the plateau edge, where $p = 1$ corresponds to a Gaussian profile and $p = 4$ was chosen in the following simulations.

The parameters a_0 (which is related to the density perturbation amplitude $\delta n/n_0$ as discussed in Appendix A), r_0, w_0, a_1 for the initial condition and $a_{\min}, R_0, \tau_e, B_0, q_s, m_i$ for the simulation conditions are chosen as specified in table 1, with the ion Larmor radius ρ_i and the perturbation wavevector k_{pert} assuming different values in the following sections. Through the choice of $\tau_e = T_e/T_i = 3 < 5.45$ the first MI condition, (3.5), i.e. $\mathcal{G} > 0$ (anomalous dispersion, self-focusing NLSE) is satisfied. The geometry of the tokamak with an aspect ratio of $R_0/a_{\min} = 10$ has a high cylindricity, which more closely resembles the NLSE model where the geometry is not considered in the equations.

The GAM damping is known to decrease with rising safety factor q_s (Palermo *et al.* 2016). In order to fulfil the assumption of weak damping (compared with the MI growth rate γ_{MI}, (3.8)) that was posed in §1, the safety factor $q_s = 15$ is chosen. In this regime the damping term derived by Qiu *et al.* (2009) is applicable as the assumptions of $1/q_s^2 \ll k_r^2 \rho_i^2 \ll 1$ and $\frac{1}{2}\tau_e k_r^2 \rho_i^2 \ll 1$ are satisfied for all of the chosen perturbation wavevectors k_{pert} (note that for $\rho_i/a_{\min} = 5.025 \times 10^{-3}$ and $k_r = 10(2\pi/a_{\min})$ the value of $\frac{1}{2}\tau_e k_r^2 \rho_i^2 \approx 0.1$ and for $k_r = 14(2\pi/a_{\min})$, $\frac{1}{2}\tau_e k_r^2 \rho_i^2 \approx 0.3$). We remark that GAM damping

Initial Condition		Tokamak plasma	
Parameter	Value	Parameter	Value
a_0	2–3.4×10^{-4} (a.u.)	$a_{\min}$	$0.13\,\mathrm{m}$
$\delta n/n_0$	2–3.4×10^{-4}	R_0	$1.3\,\mathrm{m}$
r_0	$0.6\,a_{\min}$	B_0	$1.9\,\mathrm{T}$
w_0	$0.35\,a_{\min}$	τ_e	3
p	4	m_i	$1\,\mathrm{a.m.u.}$
a_1	0.1	q_s	15
k_{pert}	4–$14\,\frac{2\pi}{a_{\min}}$	$\rho_s/a_{\min}$	$\frac{2}{425} - \frac{2}{325}$
		$\rho_i/a_{\min}$	3.842–5.025×10^{-3}

TABLE 1. Parameters used in the GK (ORB5) and NLSE simulations.

has also been studied under different approximation limits, e.g. by Sugama & Watanabe (2006) whose expression is appropriate in the limit $k_r^2 \rho_i^2 \ll 1/q_s^2$, and by Gao *et al.* (2006), who employ the approximation $\tau_e \to 0$. For a detailed discussion about the damping behaviour in the transitory regime between the limits by Qiu *et al.* (2009), Sugama & Watanabe (2006) and Gao *et al.* (2006) the reader is referred to Zonca & Chen (2008). One obtains from Qiu *et al.* (2009) that the unmodulated packet and wavevectors $k_r < 5(2\pi/a_{\min})$ are undamped (see figure 10). However, damping rates of larger wavevectors, e.g. $\gamma_{\mathrm{Qiu}}(k_r = 10(2\pi/a_{\min})) = -6.07 \times 10^{-6}\,\omega_{ci}$ are of similar orders of magnitude as the MI growth rate $\gamma_{\mathrm{MI}}(k_r = 10(2\pi/a_{\min})) = 3.11 \times 10^{-5}\omega_{ci}$, i.e. $|\gamma_{\mathrm{Qiu}}| \approx \frac{1}{5}|\gamma_{\mathrm{MI}}|$, which leads to the conclusion that damping may slow the growth of MI down but it is not expected to suppress MI.

5.1. *General comparison between NLSE and GK simulations*

A first comparison between NLSE and GK simulations of the general GAM dynamics (without modulation of the initial condition and thus without MI) was made using the parameters in table 1. Specifically, the initial GAM electric field amplitude $a_0 = 2.5 \times 10^{-4}$ (a.u.), sound Larmor radius $\rho_s/a_{\min} = 2/375$ and ion Larmor radius $\rho_i/a_{\min} \approx 4.355 \times 10^{-3}$ (where ρ_i and ρ_s are determined as described in (A1) and (A2)) were chosen as a starting point. The dispersion coefficient $\mathcal{G}$ is obtained according to (2.8) and α_{NL} is chosen as described in Appendix A (with $r = r_0 = 0.6a_{\mathrm{tok}}$). Figure 7 presents the GK and NLSE simulation results.

The comparison in figure 7 shows that, despite the uniform plasma background and thus (according to the equations introduced in § 2.1) constant values of $\mathcal{F}$ and $\mathcal{G}$, the frequency of the nonlinear GAM is radially varying in the GK simulations. This major discrepancy between the NLSE and GK simulation results may be explained by a radial dependence of α_{NL} that stems from the geometry of the tokamak. This is not included in the NLSE used in this paper since, as mentioned in § 2.1, the NLSE model for GAMs has not yet been derived from analytic theory. The dependency is analysed numerically in more detail in Appendix A and will be considered in future work.

Next, an initial condition with a modulated envelope is considered. From the parameters $a_0 = 2.5 \times 10^{-4}$ (a.u.), α_{NL} and $\mathcal{G}$ one obtains the range of unstable perturbation wavevectors k_{pert} through (3.6) as

$$|k_{\mathrm{pert}}| < |k_{\mathrm{lim}}| \approx 14.6\frac{2\pi}{a_{\min}} = \sqrt{2} \cdot k_{\max} \approx \sqrt{2} \cdot 10.3\frac{2\pi}{a_{\min}}. \qquad (5.2)$$
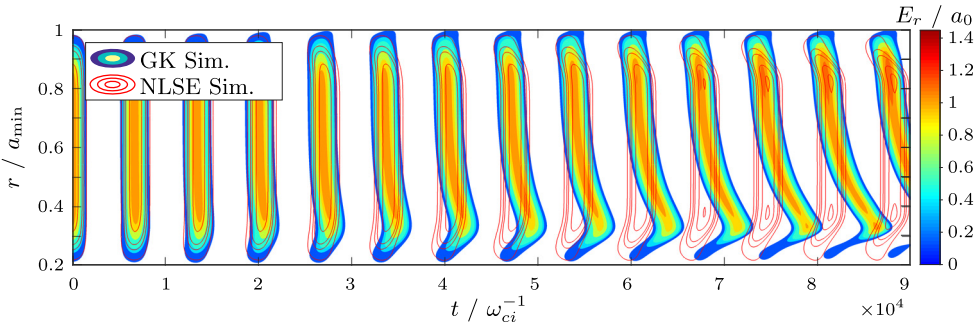
FIGURE 7. The GAM radial electric field E_r in an ORB5 GK (colour contours) and NLSE (red levels) simulation of an initially unmodulated GAM. While the frequency of the oscillation matches well at the packet centre and further outward (for $r \geq 0.6a_{min}$), differences increase when moving to smaller values of r. Since the plasma parameters were chosen to be constant across the radial coordinate r, these discrepancies can be attributed to an influence of the tokamak geometry on the nonlinear parameter α_{NL}, which is analysed in Appendix A.

It follows that the wave is unstable to MI when the wavelength of the perturbation $\lambda_{pert} = 2\pi/k_{pert}$ is larger than approximately 1/15th of the minor tokamak radius, and the maximum growth rate from (3.8) of $\gamma_{MI} = 3.05 \times 10^{-5}\omega_{ci}$ is achieved when the perturbation wavelength is approximately $a_{min}/10$.

A comparison of an NLSE and GK simulation with $k_{pert} = 10(2\pi/a_{min}) \approx k_{max}$ and $a_1 = 0.1$ is shown in figure 8. While again significant differences between the NLSE and GK simulations can be observed, the results illustrate that the MI does occur in GK GAM simulations. This is apparent since the maxima of the initial condition start to grow as time progresses and the phase skipping of the maxima (as described in § 3.1) compared with the background is observed e.g. for $t \approx 1.5 \times 10^5/\omega_{ci}$ at $r = 0.5a_{min}$ and for $t \approx 2.2 \times 10^5/\omega_{ci}$ at $r = 0.6a_{min}$ in figure 8(b). The observed radial difference in growth rate can be explained by the radial dependency of the nonlinear parameter α_{NL}, as from (3.4) it follows that γ_{MI} increases monotonically with α_{NL}, which gets larger for smaller values of r (as determined in Appendix A). Another discrepancy is the merging of two maxima at $r = 0.8a_{min}$ and $r = 0.9a_{min}$ in the GK simulation, which stay separated for the NLSE. This is again explained by α_{NL} decreasing with r since, according to (3.6), the wavevector with the highest growth rate depends as $k_{max} \propto \sqrt{\alpha_{NL}}$. As a consequence at $r \approx 0.85a_{min}$ smaller wavevectors (i.e. larger structures) will grow faster, thus favouring the merging of structures. Generally, one finds that across the whole radial space the growth rate and maximum amplitude in the GK simulation are significantly smaller compared with the NLSE simulation and theoretical predictions, as can be noticed comparing the colour bars in figure 8. This observation is further discussed in §§ 5.3 and 5.4.

To study the aforementioned differences in further detail the radial spectra of the results are compared, as depicted in figure 9. The spectrum of the NLSE simulation contains much larger wavevectors k_r than the GK simulation spectrum, most notably in the nonlinear saturation phase at $t \approx 1.1 \times 10^5/\omega_{ci}$ (see figure 8a). Together with the lower amplitude and growth rate, these findings indicate that a damping mechanism acting preferentially on higher wavevectors is present in the GK simulations, which is not contained in the NLSE solver. As a side note it is remarked that the NLSE spectrum extends up to wavevectors larger than $30(2\pi/a_{min})$, where the assumption $k_r^2\rho_i^2 \ll 1$ posed in § 2.1 is marginally or no longer satisfied, as e.g. $k_r^2\rho_i^2 = 0.2$ corresponds to $k_r \approx 16(2\pi/a_{min})$ for the current ion Larmor radius $\rho_i/a_{min} \approx 4.355 \times 10^{-3}$. One can also notice in figure 9 that higher spectral
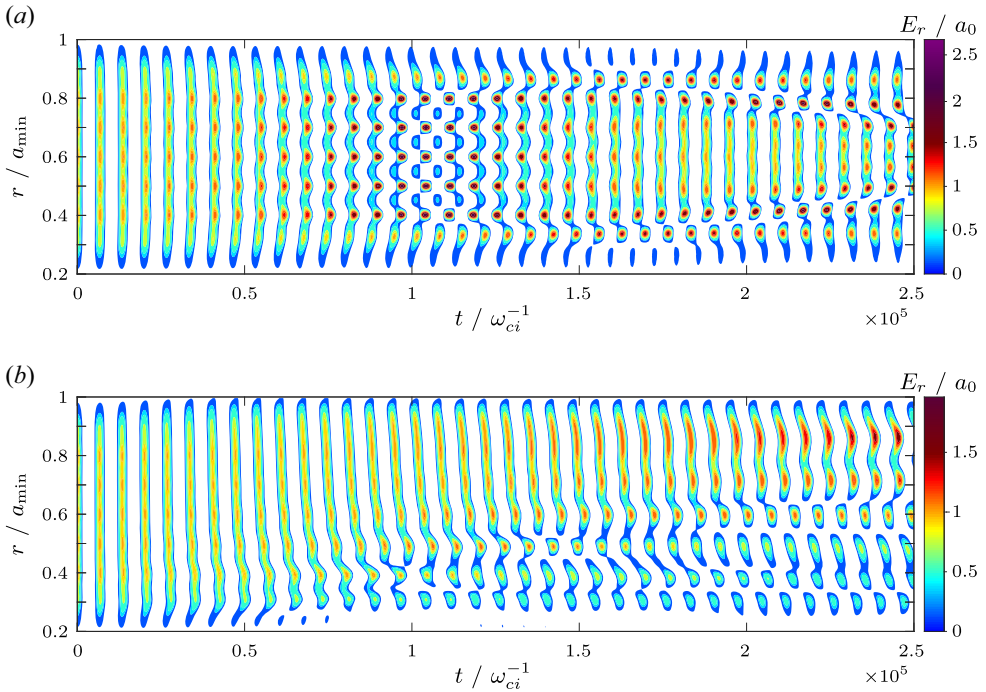
FIGURE 8. Comparison of a NLSE and a GK simulation where the envelopes are modulated sinusoidally with the perturbation wavevector $k_{pert} = 10(2\pi/a_{min}) \approx k_{max}$. The figures depict the GAM radial electric field E_r, which in the NLSE model is the real part of the wavefunction $Re[\psi] = E_r$. While the growth of the modulation is observable in both simulations, the growth rate appears to be significantly lower in the GK result compared with the NLSE simulation. One can find further discrepancies, e.g. the two individual maxima that form in the NLSE simulation at $r = 0.8a_{min}$ and $r = 0.9a_{min}$ are seemingly merged together in the GK simulation. Panels show the (*a*) NLSE simulation result and (*b*) the GK simulation result.

components develop later in ORB5 simulations as compared with the NLSE solution. This is due to the fact that the instability develops on a slower scale in GK simulations, in particular at larger r.

5.2. *Damping term*

This section gives a short introduction to the damping term derived in Qiu *et al.* (2009), which, as mentioned in § 5, can be applied to the radial GAM spectrum when electrons are considered to be adiabatic, $1/q_s^2 \ll k_r^2\rho_i^2 \ll 1$ and $\frac{1}{2}\tau_e k_r^2\rho_i^2 \ll 1$. The condition $1/q_s^2 \ll k_r^2\rho_i^2$ is always satisfied for the chosen safety factor $q_s = 15$ and the wavevectors k_{pert} of the initial perturbation. Furthermore, due to $\tau_e = 3$ the remaining requirements can be merged as follows:

$$k_r^2\rho_i^2 < \frac{\tau_e}{2}k_r^2\rho_i^2 = \frac{3}{2}k_r^2\rho_i^2 \ll 1. \tag{5.3}$$

Taking $0.3 \ll 1$ as the boundary value for the validity of this assumption, one finds that, for the largest ion Larmor radius used in this paper, $\rho_i/a_{min} = 5.025 \times 10^{-3}$, the applicability of the damping term is limited to wavevectors $k_r \lesssim 14.2(2\pi/a_{min})$. The term is given by
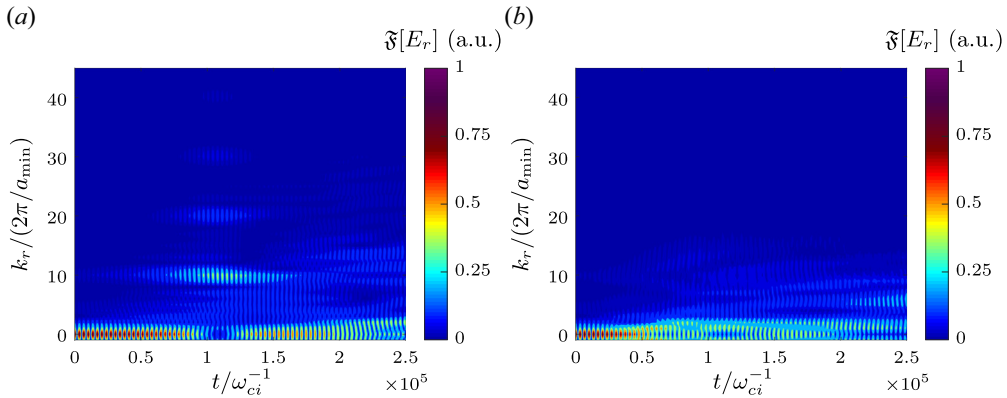
(a)   (b)

FIGURE 9. Comparison of the radial spectrum of the GK and NLSE simulations reported in figure 8. The figures show the absolute value of the radial Fourier transform of the GAM radial electric field, $|\mathfrak{F}[E_r]|$. It is apparent that the GK spectrum is in general more restrained to small wavevectors compared with the NLSE spectrum. This is especially noticeable in the saturation phase at $t \approx 1.1 \times 10^5/\omega_{ci}$, which as described in § 3 is (according to the NLSE predictions) associated with a spectrum that contains high wavevector components. Panels show the (a) NLSE radial spectrum and (b) the GK radial spectrum.

the following expression:

$$
\begin{aligned}
\gamma_{\text{Qiu}} = {} & -\frac{|\omega_b|}{\sqrt{2}b} \exp\left\{-\sigma\frac{\omega_b}{\omega_{\text{dt}}}\right\}\left[1 + b\frac{v_{Ti}^2}{\omega_b^2 R_0^2}\left(\frac{31}{16} + \frac{9}{4}\tau_e + \tau_e^2\right)\right. \\
& - b\frac{v_{Ti}^4}{\omega_b^4 R_0^4}\left(\frac{747}{32} + \frac{481}{32}\tau_e + \frac{35}{8}\tau_e^2 + \frac{1}{2}\tau_e^3\right) - 2\frac{v_{Ti}^4}{\omega_b^4 R_0^4 q_s^2}\left(\frac{23}{8} + 2\tau_e + \frac{1}{2}\tau_e^2\right)\right] \\
& \times \left\{1 + \frac{1}{24}\omega_b\omega_{\text{dt}}^2\left(-\sigma\frac{4}{\omega_{\text{dt}}^3} + \frac{\omega_b}{\omega_{\text{dt}}^4}\right) + \sigma\frac{\omega_{\text{dt}}}{\omega_b}\tau_e + \left(\tau_e^2 + \frac{5}{4}\tau_e + 1\right)\frac{\omega_{\text{dt}}^2}{\omega_b} - 2b\right\},
\end{aligned}
\tag{5.4}
$$

where the components are defined as

$$
b = k_r^2 \rho_i^2/2,
\tag{5.5}
$$

$$
v_{Ti} = \sqrt{2T_i/m_i},
\tag{5.6}
$$

$$
\begin{aligned}
\omega_b = {} & \sqrt{\frac{7}{4} + \tau_e}\frac{v_{Ti}}{R_0}\left\{1 - \frac{b}{2}\left(\frac{31}{16} + \frac{9}{4}\tau_e + \tau_e^2\right)\left(\frac{7}{4} + \tau_e\right)^{-1}\right. \\
& + \frac{b}{2}\left(\frac{747}{32} + \frac{481}{32}\tau_e + \frac{35}{8}\tau_e^2 + \frac{1}{2}\tau_e^3\right)\left(\frac{7}{4} + \tau_e\right)^{-2} \\
& \left. + \frac{1}{2q_s^2}\left(\frac{23}{8} + 2\tau_e + \frac{1}{2}\tau_e^2\right)\left(\frac{7}{4}\tau_e\right)^{-2}\right\},
\end{aligned}
\tag{5.7}
$$

$$
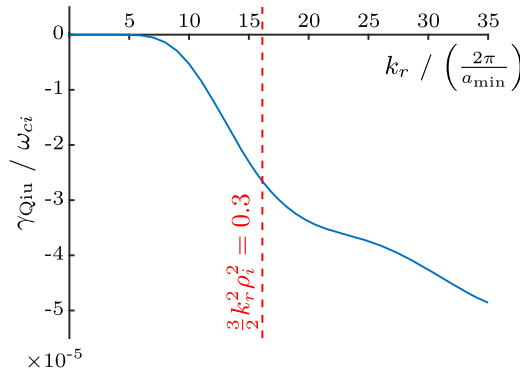\omega_{\text{dt}} = \frac{v_{Ti}}{R_0}k_r\rho_i,
\tag{5.8}
$$

FIGURE 10. Damping term for the parameters given in table 1, with $\rho_s/a_{\min} = 2/375$, $\rho_i/a_{\min} = 4.355 \times 10^{-3}$. The red line illustrates the point $\frac{3}{2}k_r^2\rho_i^2 = 0.3$ beyond which the expression may not be applicable anymore. It can be observed that the slope of the damping expression changes roughly where the line is located, which can be an indicator that after this point the behaviour is unphysical. It is remarked that the high end of the perturbation wavevectors unstable to MI, i.e. for $k_{\mathrm{pert}} = 14(2\pi/a_{\min})$, is very close to the damping applicability limit at $k_r \approx 16(2\pi/a_{\min})$.

$$\omega_{\mathrm{tt}} = \frac{v_{Ti}}{R_0 q_s}, \tag{5.9}$$

$$\sigma = \mathrm{sgn}\left[\frac{\omega_{\mathrm{b}}}{\omega_{\mathrm{dt}}}\right]. \tag{5.10}$$

This damping term describes the collisionless Landau damping of the GAM and can be applied to larger wavevectors k_r than e.g. the term derived by Sugama & Watanabe (2006), which is achieved by including higher-order harmonics of the ion transit resonances in the derivation. The resulting dependency is depicted in figure 10 for the parameters from table 1 (notably with $\rho_s/a_{\min} = 2/375$, $\rho_i/a_{\min} = 4.355 \times 10^{-3}$). It is apparent that the strength is negligible for wavevectors $k_r < 5(2\pi/a_{\min})$, but increases rapidly at $k \approx 10(2\pi/a_{\min})$.

5.3. *Role of the perturbation wavelength*

This section analyses the influence of the perturbation wavelength $\lambda_{\mathrm{pert}} = 2\pi/k_{\mathrm{pert}}$ chosen in the initial condition of the GAM radial electric field E_r on MI growth (as predicted by (3.7), see figure 5). Additionally, the damping mechanism introduced in the previous section is taken into account. Similarly to the previous section, the parameters from § 5.1 are used and consequently all perturbation wavevectors $k_{\mathrm{pert}} < 14.6(2\pi/a_{\min}) = k_{\mathrm{lim}}$ should be susceptible to MI. Thus, simulations with modulation wavevectors in the range $4 - 14(2\pi/a_{\min})$ are analysed in this section.

In order to obtain a quantitative measure of the growth (or damping) γ of the sinusoidal perturbation, the radial Fourier transforms of the GK simulation results, $\mathfrak{F}[E_r](k_r, t)$, are calculated using the fast-Fourier-transform algorithm. The Fourier coefficient corresponding to the perturbation wavevector k_{pert}, $\mathfrak{F}[E_r](k_r = k_{\mathrm{pert}}, t)$, is then extracted and an exponential fit is applied to the region of exponential MI growth or exponential decay. Due to the fact that the growth rate depends on α_{NL}, which in turn depends on the radial position r, the Fourier coefficient of the whole packet would return a complex mixture of the different growth stages at the different radial positions. As a
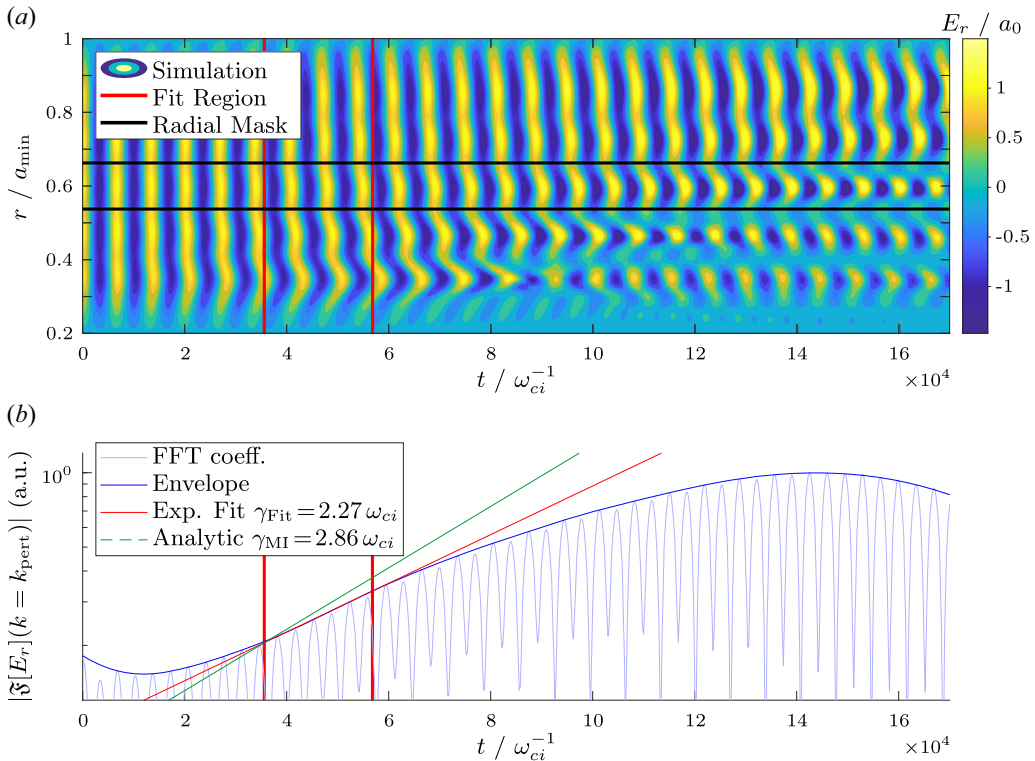
FIGURE 11. Scheme for determining the growth rate γ of the perturbation in the GK GAM simulations. The upper picture depicts the radial electric field of the case with $k_{pert} = 8(2\pi/a_{min})$. The bottom picture depicts the absolute value of the Fourier coefficient at $|\mathfrak{F}[E_r](k_r = 8(2\pi/a_{min}), t)|$ and the envelope of the coefficient. The exponential fit is applied only to the region where the growth rate is highest, as for the first oscillation cycles the GAM electric field is experiencing an initial transient where higher GAM harmonics that were excited by the initial 'drop-in' are still fading away, and for higher values of t the assumption that the perturbation amplitude a_1 is small compared with the plateau amplitude a_0 is not fulfilled anymore. (*a*) The GAM radial electric field E_r from a GK simulation with perturbation wavevector $k_{pert} = 8(2\pi/a_{min})$. The red lines show the time window where the fit was applied, the black lines indicate the radial region that was included in the calculation of the Fourier coefficient. (*b*) Time evolution of the absolute value of the Fourier coefficient of the perturbation wavevector $k_{pert} = 8(2\pi/a_{min})$. The red lines indicate the time window where the fit was applied.

consequence, before the Fourier transform is performed, a mask is applied such that only the simulation data around each maximum of the wavefront are included. This scheme is illustrated for the example of $k_{pert} = 8(2\pi/a_{min})$ in figure 11.

The aforementioned scheme, illustrated in figure 11, is applied to all simulations, with respective wavevectors $k_{pert} = 4, 5, \ldots, 14(2\pi/a_{min})$. In figure 12, the MI growth rates obtained from the GK simulation data employing the method described above are compared with the theoretical results of § 3 (see figure 5 and (3.7)). The theoretical MI predictions, which do not contain damping, clearly overestimate the GK MI growth rate γ for high perturbation wavevectors $k_{pert} > 6(2\pi/a_{min})$. As can be seen in figure 12(*a*), even when the nominal damping rate following (5.4) is included the growth rate of the MI is overpredicted as compared with the GK simulations. However, after adjusting the strength
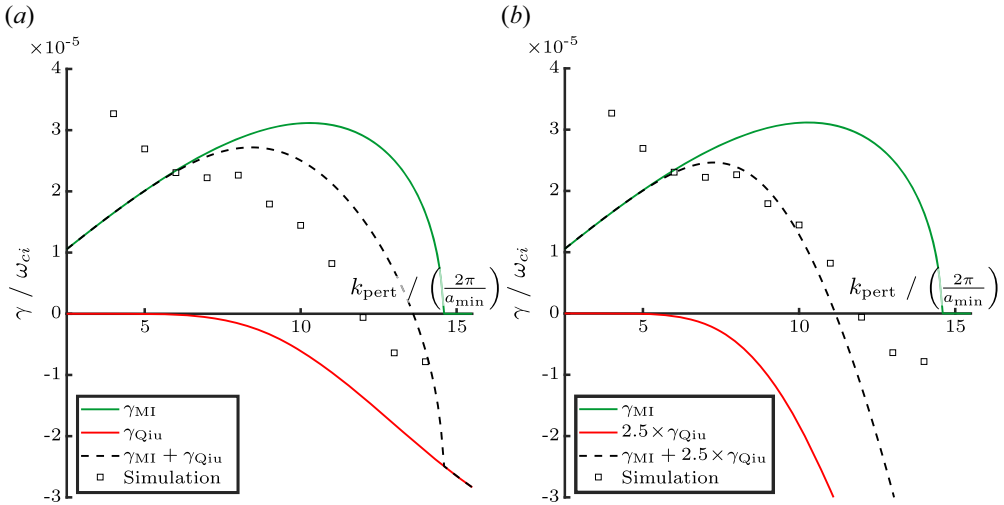
FIGURE 12. The GAM perturbation growth and damping rates γ in GK simulations where the initial condition was modulated with different perturbation wavevectors k_{pert}. The GK results were obtained via the method illustrated in figure 11. The left figure shows the comparison of the simulation results with the theoretical predictions for the analytic MI growth rate γ_{MI} (3.4), and the damping γ_{Qiu} (5.4). The theoretical predictions are found to overestimate the growth rate significantly, as seen in figure 12(*a*). The right figure establishes that, when the damping term is amplified by a factor of 2.5, data for the wavevectors in the region $6(2\pi/a_{\text{min}}) \leq k_{\text{pert}} \leq 11(2\pi/a_{\text{min}})$ more closely match the theoretical predictions. (*a*) Unmodified damping according to γ_{Qiu}. (*b*) Damping multiplied by a factor of 2.5.

of the damping amplitude by multiplying it with a factor of 2.5, the simulation results show good agreement with the theoretic predictions (figure 12*b*). Not only does this adjustment improve the matching of the threshold between stable and unstable perturbations at $k_{\text{pert}} \approx 11(2\pi/a_{\text{min}})$, but it furthermore fits better to the values of the growth rates for the wavevectors in the domain $6(2\pi/a_{\text{min}}) \leq k_{\text{pert}} \leq 11(2\pi/a_{\text{min}})$. We remark that this correction factor is also in line with the benchmark in Biancalani *et al.* (2017) (see figure 4(*b*) in this reference), where a similar difference between numeric simulations and theoretical prediction has been observed.

In contrast to the well-matching growth rates at medium wavevectors, the matching becomes poorer at larger and smaller k_{pert}, as is apparent in figure 12(*b*). For wavevectors $k_{\text{pert}} > 11(2\pi/a_{\text{min}})$, the MI is damped in GK simulations and its time behaviour is more prone to fitting errors due to the initial transient process. Additionally, these values are close to the applicability limit $\frac{3}{2}k_r^2\rho_i^2 \ll 1$ of the damping term. On the other hand, the growth rates obtained from the GK simulations at the lower end, with $k_{\text{pert}} < 6(2\pi/a_{\text{min}})$, are too high compared with theory. Further investigations regarding this discrepancy are needed.

5.4. *Role of the ion Larmor radius*

The last section established that the small scales (high wavevectors) are more strongly affected by damping and that the analytical term from Qiu *et al.* (2009), when adjusted by a factor 2.5, gives a good approximation to the observations. This section tests this hypothesis further by analysing the impact of a change of the ion Larmor radius ρ_i on the damping scale, where the values $\rho_{i1}/a_{\text{min}} = 3.842 \times 10^{-3}$, $\rho_{i2}/a_{\text{min}} = 4.355 \times 10^{-3}$
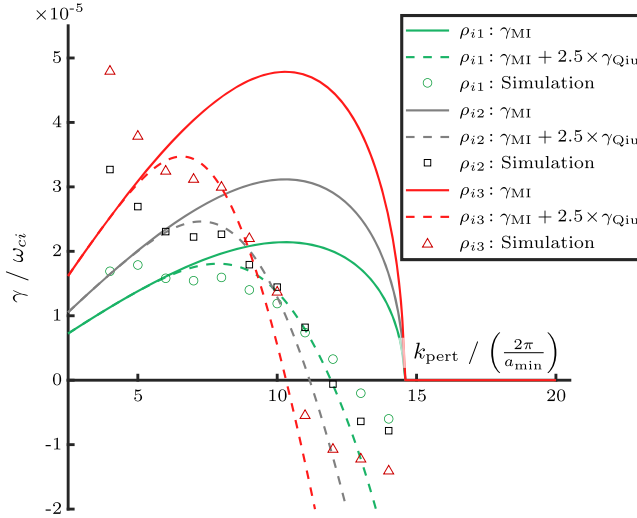
FIGURE 13. The GAM MI growth and damping rates in GK simulations with different perturbation wavevectors k_{pert} and ion Larmor radii ρ_i ($\rho_{i1}/a_{min} = 3.842 \times 10^{-3}$, $\rho_{i2}/a_{min} = 4.355 \times 10^{-3}$ and $\rho_{i3}/a_{min} = 5.025 \times 10^{-3}$) compared with the theoretical predictions from the analytic MI growth rate γ_{MI}, (3.4) and the analytic GAM damping γ_{Qiu}, (5.4). The difference in the maxima of the growth rates stems mainly from the different packet background amplitudes that were chosen according to (5.11).

(same value as in the previous sections) and $\rho_{i3}/a_{min} = 5.025 \times 10^{-3}$ were chosen for the comparison. The changes of ρ_i are achieved by adjusting the ion thermal velocity v_{Ti}, which in the simulations is determined according to (A1) and (A2). The analytic damping term γ_{Qiu} predicts that, for smaller Larmor radii, smaller scales i.e. higher wavevectors k_{pert} should be less damped.

A change of ρ_i (via v_{Ti}) influences both $\mathcal{G}$ and α_{NL}, meaning that the range of unstable wavevectors $k_{pert} < k_{lim} = 2a_0\sqrt{\alpha_{NL}/\mathcal{G}}$ from (3.6) may change. To decorrelate the change of ρ_i from the change of the unstable MI wavevectors, the parameter a_0 is selected depending on ρ_i to ensure that the range of the unstable MI wavevectors stays the same. Precisely, due to $\mathcal{G} \propto \rho_i^3$ (see (2.8) with $v_{Ti} \propto \rho_i$) and $\alpha_{NL} \propto 1/\rho_i$ (see Appendix A) one finds from (3.6) that in order to keep the unstable range constant a_0 needs to be adjusted as

$$k_{lim} = 2a_0\sqrt{\frac{\alpha_{NL}}{\mathcal{G}}} \propto \sqrt{\frac{1}{\rho_i^4}}a_0 = \text{const.} \quad \Rightarrow \quad a_0 \propto \rho_i^2. \qquad (5.11)$$

In order to obtain the same $k_{lim} = 14.5(2\pi/a_{min})$ as in the previous sections the corresponding amplitudes are $a_{01} \approx 1.99 \times 10^{-4}$ (a.u.), $a_{02} \approx 2.56 \times 10^{-4}$ (a.u.) and $a_{03} \approx 3.40 \times 10^{-4}$ (a.u.) for ρ_{i1}, ρ_{i2} and ρ_{i3}, respectively. The simulations were analysed with the scheme introduced in the last section with the corresponding growth and damping rates presented in figure 13.

The results confirm the findings of the previous section that the adjustment by a factor of 2.5 of the amplitude of the damping term does reproduce the observed damping rate. Additionally, the theoretical predictions for the change of growth rates from γ_{MI} due to the changing amplitude is in good agreement with the simulation results. However, similarly to figure 12(b) the damping rate is overestimated in the region where the simulations
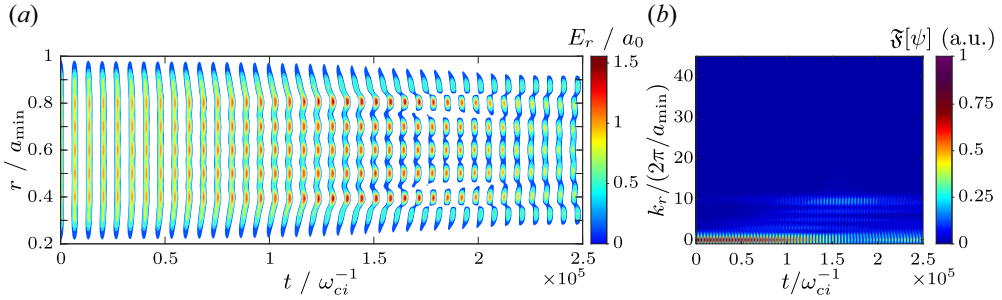
FIGURE 14. Repetition of the NLSE simulation reported in figure 8(*a*), where now the damping scheme described at the beginning of this section is included. The figure shows the time evolution of the GAM radial electric field E_r (left) as well as the corresponding radial spectrum (right), i.e. the absolute value of the radial Fourier transform of the GAM radial electric field, $|\mathfrak{F}[E_r]|$.

are damped and the growth rate results for $k_{\text{pert}} < 6(2\pi/a_{\text{min}})$ are again higher than the theoretical prediction.

5.5. *NLSE simulations including damping*

We now include the findings regarding the damping term of the previous two sections in the NLSE solver and compare a damped NLSE simulation with a GK simulation. The damping given by (5.4) is amplified by a factor 2.5 and included in the numerical solver at the point where the dispersive term is applied, i.e. (4.4) in § 4.1. However, as shown in figure 9(*a*), during the MI saturation phase large wavevectors ($k_r > 20(2\pi/a_{\text{min}})$) appear in the spectrum which, due to the condition $(\tau_e/2)k_r^2\rho_i^2 \ll 1$ from § 5.2, lie outside of the applicability range of γ_{Qiu}. From the GK simulations, see figure 9(*b*), it is clear that these high wavevectors should be strongly suppressed, which was achieved by applying $\gamma = -4 \times 10^{-4}\omega_{ci}$ to all wavevectors fulfilling $(\tau_e/2)k_r^2\rho_i^2 \geq 0.3$.

The (undamped) NLSE simulation presented in figure 8(*a*) is now repeated with the inclusion of the above described damping scheme. The damped result is reported in figure 14 together with the corresponding spectrum. A clear improvement in regards to multiple aspects can be discerned when comparing damped and undamped NLSE simulations with the related GK result from figure 8(*b*). First of all, the point in time at which the MI saturation phase appears in the simulations matches much better, with $t_{\text{sat.}}^{\text{NLSE damp.}} \approx 1.8 \times 10^5 \, 1/\omega_i$ and $t_{\text{sat.}}^{\text{GK}} \approx 2.2 \times 10^5 \, 1/\omega_i$ (at the packet centre $r = r_0 = 0.6a_{\text{tok}}$), compared with the undamped NLSE simulation from figure 8(*a*) with $t_{\text{sat.}}^{\text{NLSE undamp.}} \approx 1.1 \times 10^5 \, 1/\omega_i$. Furthermore, the maximal amplitude at the centre $r = r_0$ is in better agreement, with $E_{\text{max}}^{\text{NLSE damp.}} = 1.31a_0$ and $E_{\text{max}}^{\text{GK}} \approx 1.26a_0$, compared with $E_{\text{max}}^{\text{NLSE undamp.}} = 2.43a_0$. The growth rate is $\gamma^{\text{NLSE damp.}} \approx 1.48 \times 10^{-5}\omega_{ci}$, which is very similar to the value obtained for the GK simulation with $\gamma^{\text{GK}} \approx 1.41 \times 10^{-5}\omega_{ci}$. However, a spectral comparison between figures 14 and 9(*b*) illustrates significant differences, notably that the GK spectrum is much more complex, with more interactions of the different wavevectors. This may in part stem from the radial dependence of the value of α_{NL}, which leads to incoherent phase fronts in the GK simulations and is not included in the NLSE simulation (see also discussion in § 5.1), on the other hand, it may also be a consequence of the generally reduced complexity of the NLSE model.
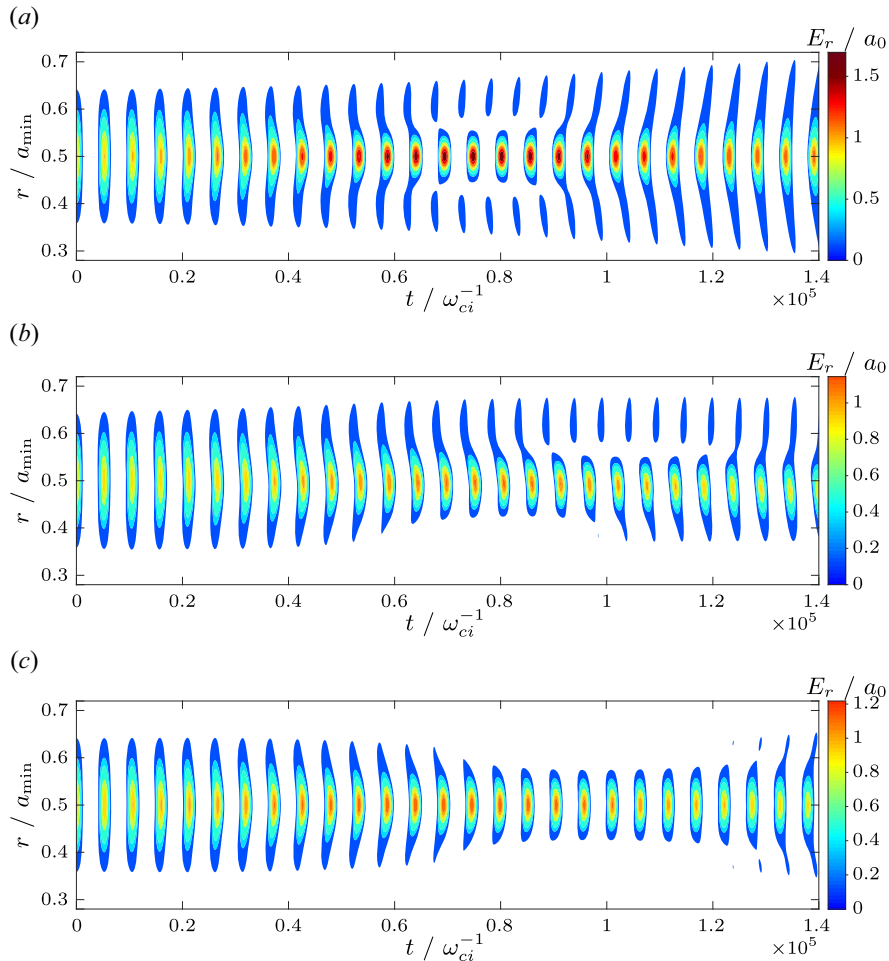
FIGURE 15. Comparison of the evolution of the GAM radial electric field E_r with an unperturbed Gaussian initial condition according to the undamped NLSE, damped NLSE and GK theory. The plasma background parameters of the simulations are $\tau_e = 2$, $q_s = 11$, $\rho_i/a_{\min} = 3.784 \times 10^{-3}$, the initial condition is given by (5.1) with $a_0 = 3 \times 10^{-4}$ (a.u.), $a_1 = 0$, $w_0 = 0.1 a_{\min}$ and $p = 1$. (*a*) The NLSE simulation result. (*b*) The GK simulation result. (*c*) The damped NLSE simulation result.

5.6. *Self-focusing of Gaussian packets*

This section illustrates the self-focusing effect of the NLSE on an unmodulated initial condition where for the envelope a Gaussian packet is chosen. As detailed in § 2.2, self-focusing is observed for anomalous dispersion, i.e. $\mathcal{G} > 0$ and $\tau_e \lesssim 5.45$. The resulting comparison between a GK, an undamped NLSE and a damped NLSE (as specified in § 5.2) simulation is presented in figure 15.

One can observe that, in all three simulations, the Gaussian packet experiences self-focusing, resulting in an increase of the maximal amplitude and a phase skip of the Gaussian centre compared with the packet edges. It is apparent that this behaviour is very similar to the MI, while it in contrast does not require an initial modulation of the envelope. We should note at this point that, differently from the standard scenario of the
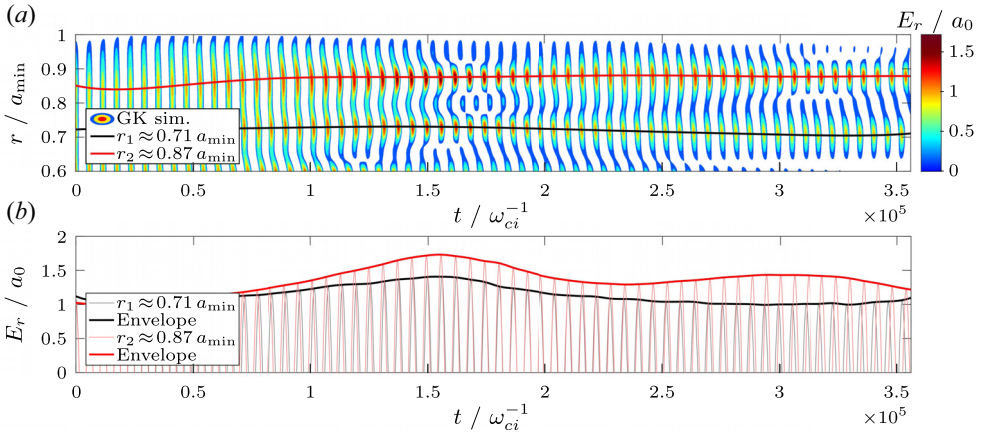
FIGURE 16. Gyrokinetic simulation of a GAM which shows the breather behaviour of the MI. The upper figure shows the radial electric field E_r with its radial shape, the bottom figure shows the value of E_r along the lines shown in the upper figure, which follow the maxima. The red curve shows two MI saturation phases, the first at $t \approx 1.7 \times 10^5 \ 1/\omega_{ci}$ and the second one at $t \approx 3.3 \times 10^5 \ 1/\omega_{ci}$. The black curve shows the start of a second MI growth phase at the end of the simulation. The parameters are chosen as specified in table 1, with $\rho_{i3}/a_{min} = 5.025 \times 10^{-3}$, $a_0 = 3.4 \times 10^{-4}$ and $k_{pert} = 8(2\pi/a_{min})$.

MI presented in § 3.1, the background wave is not a plane wave but a packet with a finite spectrum. Hence, it contains also higher spectral components, which can act as a seed for MI. Indeed, a spectral analysis, which for the sake of brevity is not reported here, reveals exponential growth of the wavevectors $k_r = 3(2\pi/a_{min})$, $4(2\pi/a_{min})$ and $5(2\pi/a_{min})$. This observation suggests an interpretation of this behaviour as an MI, whereas the observed unstable wavevectors are not necessarily the ones with the strongest growth rates but also depend on the initial conditions of the packet. We should add that the generation of higher spectral components is an inherent part of the nonlinear dynamics of the GAM, which might contribute to the observed spectral behaviour on top of the MI.

Similarly to § 5.2 it is observed that, with damping included in the NLSE model, the maximum amplitude of the GK simulation is more closely reproduced. Furthermore one finds better agreement for the width and steepness of the focused packet, i.e. in the GK and damped NLSE simulations at $t \approx 1.1 \times 10^5 \ 1/\omega_i$ compared with the undamped NLSE at $t \approx 0.8 \times 10^5 \ 1/\omega_i$. The radial asymmetry that develops in the GK simulation is not found in the NLSE simulations and can be explained by the radial dependence of α_{NL} that was introduced in § 5.1 and is explored further in Appendix A.

5.7. *Breather simulations*

In this section the phenomenon of the Akhmediev breather is studied in GK simulations. Akhmediev breathers (ABs) (Akhmediev & Korneev 1986) are special types of MI solutions to the NLSE which predict that after the saturation phase, the MI initial condition is restored, as illustrated in figure 4, and new MI growth should be observable. This phenomenon is hard to observe in GK simulations as e.g. the dependency of α_{NL} breaks the packet apart and hinders the return to the initial condition after the first saturation phase. As a consequence, we concentrate on the region $r > 0.6a_{min}$, where the results from Appendix A predict only small changes of α_{NL}. A GK simulation with a breather solution is depicted in figure 16.

The maximum at $r_2 \approx 0.87a_{min}$ experiences two saturation phases, the first one at $t \approx 1.5 \times 10^5 \omega_{ci}^{-1}$ and the second at $t \approx 3.3 \times 10^5 \omega_{ci}^{-1}$, thus demonstrating the AB phenomenon for a GAM packet in a GK simulation. Comparable behaviour happens for the maximum at $r \approx 0.71$, however, the growth is slower and not as pronounced. The impact of the damping mechanism and the differences in the nonlinear coefficient α_{NL} are again present in the simulations: for example, the second saturation phase at $t \approx 3.3 \times 10^5 \omega_{ci}^{-1}$ of the maximum centred around r_2 is observed to have a maximum amplitude of $1.44a_0$, which is significantly lower than the value of $1.74a_0$ found in the first saturation phase, whereas an undamped AB would under ideal conditions yield the same maximum value in both saturation phases.

While more complex patterns of the AB are possible under ideal conditions, such as the appearance of growth phases of other unstable wavevectors in between the saturation phases of the initial perturbation wavevector k_{pert}, see e.g. Copie, Randoux & Suret (2020), the deviations from a pure NLSE-like behaviour due to the mechanisms introduced in the previous sections make the possibility of such observations highly unlikely.

6. Summary and conclusions

The results of this paper show that geodesic-acoustic oscillations (GAMs) are susceptible to modulational instability (MI) under the conditions predicted by the nonlinear Schrödinger equation (NLSE) model. However, the high wavevectors that are part of the nonlinear saturation phase and important for the MI cycle (and MI breathers, see § 5.7) do not develop in gyrokinetic (GK) simulations due to the Landau damping which was characterized in detail in §§ 5.2–5.5. For the parameters considered in this study the aforementioned damping effect hinders the MI process significantly from developing to its full extent and is strong enough to stabilize some of the (according to the undamped NLSE model) unstable wavevectors, as was illustrated in figure 13 for $k \gtrsim 12(2\pi/a_{min})$. A second significant shortcoming of the NLSE model was the assumption that α_{NL} is independent of the radial coordinate r. The GK simulations of this paper establish the radial variation of the nonlinear coefficient $\alpha_{NL} = \alpha_{NL}(r)$ of the NLSE model for GAMs, which was not evident in the prior study on this topic (Poli *et al.* 2021), due to the relatively narrow Gaussian packets that were considered there.

One can conclude from the theoretical descriptions of the MI and the damping mechanism ((3.7) and (5.4), respectively) that GAM MI is more likely to be observable for high safety factors and small Larmor radii (i.e. low ion temperatures T_i and thermal velocities v_{Ti}). Theory further suggests that the tokamak aspect ratio $A = R_0/a_{min}$ may have an impact on the GAM MI growth rate, however, further investigations on the dependency of the nonlinear coefficient α_{NL} on the geometric parameters are needed to confirm this prediction.

The observed significance of damping in the GK simulation results might seem surprising as the initial spectrum of the packet lies in a range for which theory predicts negligible damping. This enhanced damping observed in the GK simulations is akin to the phenomenon analysed in detail in Palermo *et al.* (2016) and Biancalani *et al.* (2016). There, the generation of higher wavevectors through linear processes due to the presence of radially non-uniform profiles was found to increase GAM damping significantly, leading to the inclusion of a 'phase-mixing damping adjustment'. Similarly to these findings, as was discussed in § 3.1, the MI process is associated with the (in our case nonlinear) generation of high wavevector components in the radial GAM spectrum. This interpretation of the simulation results is confirmed by the good agreement they exhibit with an NLSE model corrected with the inclusion of the damping rate derived in Qiu *et al.* (2009), as is

presented in § 5.5. The overall correction factor adopted here to achieve a quantitative matching with the GK simulations is in line with previous findings (Biancalani *et al.* 2017).

While the NLSE model proved to give accurate predictions of the general GAM behaviour, the exact dynamics shows significant differences. An improvement of the model, putting it on a more firm theoretical ground, requires a derivation of the NLSE equation for GAMs from first principles, which should be addressed in the near future. Predictive capability to other parameter regimes is limited and will only improve with further studies on the unknown variable α_{NL}.

Altogether, the results indicate that (without considering interactions with other plasma modes) the possibility and impact of an MI on the GAM dynamics will be small. This conclusion becomes more evident by the fact that in this study, electrons were treated adiabatically in simulations and in the damping term, while recent research suggests that a kinetic treatment of the electrons will increase damping, thus decreasing the likeliness of MI even further (Zhang & Lin 2010; Ehrlacher *et al.* 2018). On the other hand, the self-focusing behaviour associated with the MI formation process is omnipresent in the regime of anomalous dispersion ($\mathcal{G} > 0$, $\tau_e \lesssim 5.45$) and may be observable in other simulations similarly to the case presented in § 5.6. The main reason behind this is the size of the involved structures and unstable wavevectors k_r: while the self-focusing effect only requires that a local maximum is present in the packet envelope, which can be of any size (or even simply the packet itself), MI formation requires that the maximum is 'on top of' a relatively constant packet, thus demanding much finer structures and higher wavevectors. This is not only a much more unlikely initial condition to spontaneously develop in a tokamak, but is also much more significantly affected by the damping process illustrated in §§ 5.2–5.4. However, this conclusion is only valid in the absence of interaction with other plasma modes.

Acknowledgements

Funding

Declaration of interests

The authors report no conflict of interest.

Data availability statement

The data that support the findings of this study are available from the corresponding author upon reasonable request.

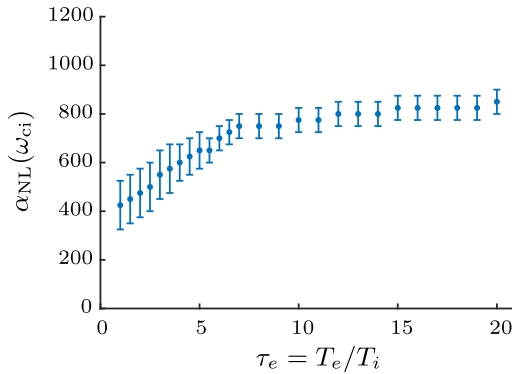FIGURE 17. Dependency of the nonlinear parameter α_{NL} on the electron-to-ion temperature ratio τ_e. The remaining parameters were chosen as specified in table 1, with $\rho_i/a_{\mathrm{min}} = 3.842 \times 10^{-3}$, $q_s = 5$ and $r_0 = 0.5 a_{\mathrm{min}}$.

Appendix A. Determination of α_{NL}

In order to make meaningful predictions about the MI behaviour and growth rates γ_{MI} (see (3.7)), it is necessary to assess the magnitude of the strength α_{NL} of the nonlinear term. Since an analytical expression for this parameter has currently not yet been derived, as was already mentioned in §2.1, its value is in this study determined by comparing NLSE results with GK simulations of isolated GAMs obtained with the code ORB5. The axisymmetric component of the GAM radial electric field is initialized as described in §4.2, where the NLSE evolves an initial electric field perturbation, while in ORB5 the electric field is generated from an initial perturbation δn of the ion density.

To obtain the exact value of the initial electric field perturbation from the initial density perturbation amplitude $\delta n/n_0$ one would have to evaluate the proportionality constant of the relation in (4.6). Since the exact physical values of the electric field do not matter for the results of this study and to simplify comparisons between the NLSE and GK simulations, we define a normalized amplitude of the electric field simply as $a_0 = \delta n/n_0$. As a consequence, the parameter α_{NL} is given here in units related to the amplitude of the relative density perturbation $\delta n/n_0$.

For the comparison of NLSE and GK simulations an unperturbed Gaussian envelope (i.e. $a_1 = 0$, $p = 1$ in (5.1)) was chosen for the initial condition. The dependency of α_{NL} on the electron-to-ion temperature ratio $\tau_e = T_e/T_i$, the safety factor q_s, the radial position r_0 of the GAM and the ion Larmor radius ρ_i was determined. The ion Larmor radius is set in ORB5 by the choice of the parameter L_x, which is defined through the following relations:

$$L_x = 2\frac{a_{\mathrm{min}}}{\rho_s}, \tag{A1}$$

$$\rho_s = \frac{c_s}{\omega_{ci}} = \frac{\sqrt{T_e/m_i}}{\omega_{ci}} = \sqrt{\frac{\tau_e}{2}}\frac{\sqrt{2T_i/m_i}}{\omega_{ci}} = \sqrt{\frac{\tau_e}{2}}\rho_i. \tag{A2}$$

This subsequently also affects the value of the ion temperature. The remaining parameters a_{min}, R_0, B_0, m_i were chosen as specified in table 1. The results for the dependencies on τ_e, ρ_i (i.e. L_x) and r_0 are depicted in figures 17–19, respectively. The respective error bars illustrate the range of values of α_{NL} in which the NLSE simulations matched GK results within one quarter of the oscillation period $1/4 T_{\mathrm{GAM}}$ at the end of the simulation.
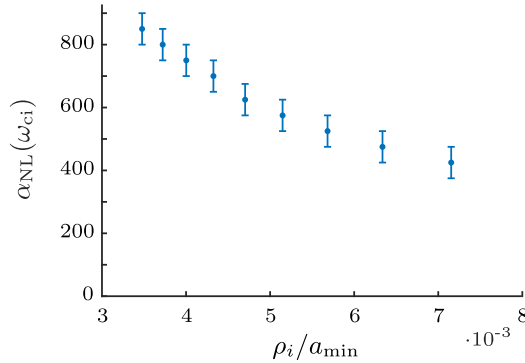
FIGURE 18. Dependency of the nonlinear parameter α_{NL} on the ion Larmor radius ρ_i. The remaining parameters were chosen as specified in table 1, with $\tau_e = 4$, $q_s = 5$ and $r_0 = 0.5a_{min}$.
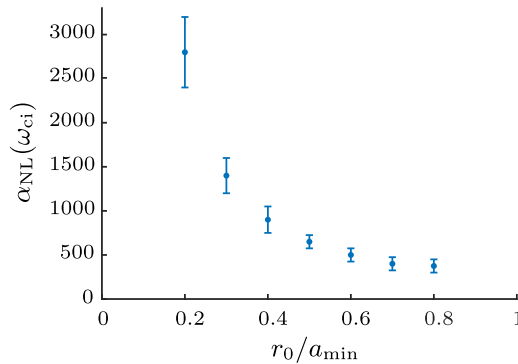

FIGURE 19. Dependency of the nonlinear parameter α_{NL} on the position r_0 of the GAM in the minor tokamak radius. This dependency was not included in the NLSE simulation dynamics. The remaining parameters were chosen as specified in table 1, with $\tau_e = 4$, $\rho_i/a_{min} = 3.842 \times 10^{-3}$ and $q_s = 5$.

From figure 17 one finds that $\alpha_{NL}(\tau_e)$ increases nearly linearly with τ_e, but with different slopes in the regime of anomalous ($\tau_e \lesssim 5.45$) and normal ($\tau_e \gtrsim 5.45$) dispersion. The error bars in the regime of anomalous dispersion are higher due to the self-focusing effect of Gaussian packets, which is discussed in § 5.6 and complicated comparisons. From figure 18 as a first approximation the proportionality $\alpha_{NL} \propto 1/\rho_i$ is obtained. The radial position of the GAM is found to heavily influence the strength of the nonlinear parameter as seen in figure 19, most notably when r_0 is below $0.4a_{min}$. For the safety factor q_s it was found that the value of α_{NL} does not change significantly in the range $q_s = 1 \ldots 15$ considered in this paper.

Appendix B. Qualitative picture for the self-focusing NLSE and MI

This section presents a qualitative explanation for the MI formation process in terms of an interaction of the between the effects of the nonlinear and the dispersive term, which were introduced in § 2.2. Although the MI is meanwhile a well-known phenomenon, we believe that the summary of this simple interpretation might be useful, in particular to interpret the results of this paper.
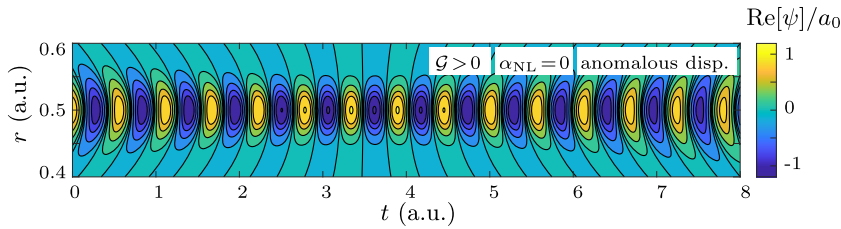
FIGURE 20. An NLSE simulation of the GAM electric field $E_r = \text{Re}[\psi]$ for a Gaussian with an initial convex curvature in (r, t)-space. The anomalous dispersion reduces the width of the Gaussian while increasing its amplitude until the phase front is flat at $t \approx 3.5$. After this point one observes the usual dispersive broadening and increase of concave curvature.

As depicted in figure 2, the effect of the dispersive term (without nonlinearity, $\alpha_{\text{NL}} = 0$) on a 'flat' phase front at $t = 0$ is an increase in width and the appearance of (in the case of anomalous dispersion concave) curvature as time progresses. When considering a packet with initial curvature opposite to what is generated by the dispersive term, one can observe that during the process of reducing the phase-front curvature, the packet width decreases until the phase front is flat, as shown in figure 20. After this point one finds the usual dispersive broadening. This is the well-known behaviour of a Gaussian pulse in optics (but with the roles of time and space reversed), see e.g. Hecht (2012). One can conclude that, in the regime of anomalous dispersion, as long as the packet curvature is convex in (r, t)-space, the width and curvature of the packet will decrease while the amplitude of the maximum increases. For normal dispersion one will observe the same effect for an initially concave packet.

As mentioned in § 2.2 the nonlinear term introduces a phase shift, described by (2.12), in regions where the amplitude is higher, which gives maxima in the packet a convex curvature, as seen in figure 3. It follows that, when both the nonlinear and (anomalous) dispersive contributions to the dynamics are considered, the dispersive term acts to reduce the curvature from the nonlinear phase shift and decreases the width of the packet. As long as the strength of the nonlinear phase shift is stronger than the effect of the dispersive term, the packet stays convexly curved. As a result, the width of the region around the maximum will decrease while its amplitude rises. This competition between the nonlinear and the dispersive term is represented mathematically by second condition for MI growth stated in the previous section (3.6), which can be rewritten to

$$\frac{\mathcal{G} k_{\text{pert}}^2}{2} < 2a_0^2 \alpha_{\text{NL}}. \tag{B1}$$

Here, the left-hand side is the strength of the phase shift of a local sinusoidal maximum due to the dispersive term, while the right-hand side is the nonlinear phase-shift of the maximum relative to its surrounding background.

REFERENCES

AGRAWAL, G. 2019 *Nonlinear Fiber Optics*, 6th edn. Academic Press.

AKHMEDIEV, N. & KORNEEV, V. 1986 Modulation instability and periodic solutions of the nonlinear Schrödinger equation. *Theor. Math. Phys.* **69** (2), 1089–1093.

BENJAMIN, T.B. & FEIR, J.E. 1967 The disintegration of wave trains on deep water. Part 1. Theory. *J. Fluid Mech.* **27** (3), 417–430.

BIANCALANI, A., BOTTINO, A., EHRLACHER, C., GRANDGIRARD, V., MERLO, G., NOVIKAU, I., QIU, Z., SONNENDRÜCKER, E., GARBET, X. & GÖRLER, T. 2017 Cross-code gyrokinetic verification

and benchmark on the linear collisionless dynamics of the geodesic acoustic mode. *Phys. Plasmas* **24**, 062512.

BIANCALANI, A., PALERMO, F., ANGIONI, C., BOTTINO, A. & ZONCA, F. 2016 Decay of geodesic acoustic modes due to the combined action of phase mixing and landau damping. *Phys. Plasmas* **23**, 112115.

BOTTINO, A. & SONNENDRÜCKER, E. 2015 Monte carlo particle-in-cell methods for the simulation of the Vlasov–Maxwell gyrokinetic equations. *J. Plasma Phys.* **81**, 435810501.

BRIZARD, A.J. & HAHM, T.S. 2007 Foundations of nonlinear gyrokinetic theory. *Rev. Mod. Phys.* **79**, 421.

CHEN, L., LIN, Z. & WHITE, R. 2000 Excitation of zonal flow by drift waves in toroidal plasmas. *Phys. Plasmas* **7** (8), 3129–3132.

CHEN, L. & ZONCA, F. 2016 Physics of alfvén waves and energetic particles in burning plasmas. *Rev. Mod. Phys.* **88**, 015008.

CONWAY, G.D., SMOLYAKOV, A.I. & IDO, T. 2021 Geodesic acoustic modes in magnetic confinement devices. *Nucl. Fusion* **62** (1), 013001.

COPIE, F., RANDOUX, S. & SURET, P. 2020 The physics of the one-dimensional nonlinear Schrödinger equation in fiber optics: Rogue waves, modulation instability and self-focusing phenomena. *Rev. Phys.* **5**, 100037.

DIAMOND, P.H., ITOH, S.-I., ITOH, K. & HAHM, T.S. 2005 Zonal flows in plasma – a review. *Plasma Phys. Control. Fusion* **47**, R35.

DUDLEY, J.M., GENTY, G., DIAS, F., KIBLER, B. & AKHMEDIEV, N. 2009 Modulation instability, akhmediev breathers and continuous wave supercontinuum generation. *Opt. Express* **17** (24), 21497–21508.

EHRLACHER, C., GARBET, X., GRANDGIRARD, V., SARAZIN, Y., DONNEL, P., CASCHERA, E., GHENDRIH, P. & ZARZOSO, D. 2018 Contribution of kinetic electrons to gam damping. *J. Phys.: Conf. Ser.* **1125**, 012010.

FAOU, E. 2012 *Geometric Numerical Integration and Schrödinger Equations*, vol. 15. European Mathematical Society.

GAO, Z., ITOH, K., SANUKI, H. & DONG, J. 2006 Multiple eigenmodes of geodesic acoustic mode in collisionless plasmas. *Phys. Plasmas* **13** (10).

HECHT, E. 2012 *Optics*. Pearson Education India.

ITOH, K., ITOH, S.-I., DIAMOND, P., HAHM, T., FUJISAWA, A., TYNAN, G., YAGI, M. & NAGASHIMA, Y. 2006 Physics of zonal flows. *Phys. Plasmas* **13** (5).

ITOH, K., ITOH, S.-I., DIAMOND, P.H., FUJISAWA, A., YAGI, M., WATARI, T., NAGASHIMA, Y. & FUKUYAMA, A. 2006 Geodesic acoustic eigenmodes. *Plasma Fusion Res.* **1**, 037.

KENGNE, E., LIU, W. & MALOMED, B.A. 2021 Spatiotemporal engineering of matter-wave solitons in Bose–Einstein condensates. *Phys. Rep.* **899**, 1–62.

KUZNETSOV, E.A., RUBENCHIK, A.M. & ZAKHAROV, V.E. 1986 Soliton stability in plasmas and hydrodynamics. *Phys. Rep.* **142** (3), 103–165.

LANTI, E., OHANA, N., TRONKO, N., HAYWARD-SCHNEIDER, T., BOTTINO, A., MCMILLAN, B.F., MISHCHENKO, A., SCHEINBERG, A., BIANCALANI, A., ANGELINO, P., *et al.* 2020 Orb5: a global electromagnetic gyrokinetic code using the pic approach in toroidal geometry. *Comput. Phys. Commun.* **251**, 107072.

MURTAZA, G. & SALAHUDDIN, M. 1982 Modulational instability of ion acoustic waves in a magnetised plasma. *Plasma Phys.* **24** (5), 451.

NGUYEN, C., GARBET, X. & SMOLYAKOV, A.I. 2008 Variational derivation of the dispersion relation of kinetic coherent modes in the acoustic frequency range in tokamaks. *Phys. Plasmas* **15**, 112502.

PALERMO, F., BIANCALANI, A., ANGIONI, C., ZONCA, F. & BOTTINO, A. 2016 Combined action of phase-mixing and landau damping causing strong decay of geodesic acoustic modes. *Europhys. Lett.* **115**, 15001.

PALERMO, F., CONWAY, G., POLI, E. & ROACH, C. 2023 Modulation behaviour and possible existence criterion of geodesic acoustic modes in tokamak devices. *Nucl. Fusion* **63** (6), 066010.

PALERMO, F., POLI, E. & BOTTINO, A. 2020 Complex eikonal methods applied to geodesic acoustic mode dynamics. *Phys. Plasmas* **27**, 032507.

PALERMO, F., POLI, E., BOTTINO, A., BIANCALANI, A., CONWAY, G.D. & SCOTT, B. 2017 Radial acceleration of geodesic acoustic modes in the presence of a temperature gradient. *Phys. Plasmas* **24**, 072503.

POLI, E., BOTTINO, A., MAJ, O., PALERMO, F. & WEBER, H. 2021 Nonlinear dynamics of geodesic-acoustic-mode packets. *Phys. Plasmas* **28**, 112505.

POLI, E., PALERMO, F., BOTTINO, A., MAJ, O. & WEBER, H. 2020 Complex-Hamiltonian paraxial description of damped geodesic acoustic modes. *Phys. Plasmas* **27**, 082505.

QIU, Z., CHEN, L. & ZONCA, F. 2009 Collisionless damping of short wavelength geodesic acoustic modes. *Plasma Phys. Control. Fusion* **51**, 012001.

QIU, Z., CHEN, L. & ZONCA, F. 2018 Kinetic theory of geodesic acoustic modes in toroidal plasmas: a brief review. *Plasma Sci. Technol*. **20**, 094004.

REMOISSENET, M. 1996 Solitons and modulational instability. *Ann. Télécommun*. **51**, 297.

SCHAMEL, H. 1975 Analytic bgk modes and their modulational instability. *J. Plasma Phys*. **13** (1), 139–145.

SCOTT, A. 2006 *Encyclopedia of Nonlinear Science*. Routledge.

SCOTT, B. 2003*a* The geodesic transfer effect on zonal flows in tokamak edge turbulence. *Phys. Lett.* A **320** (1), 53–62.

SCOTT, B.D. 2003*b* Computation of electromagnetic turbulence and anomalous transport mechanisms in tokamak plasmas. *Plasma Phys. Control. Fusion* **45**, A385.

SCOTT, B.D. 2005 Energetics of the interaction between electromagnetic exb turbulence and zonal flows. *New J. Phys*. **7**, 92.

SMOLYAKOV, A.I., BASHIR, M.F., EFIMOV, A.G., YAGI, M. & MIYATO, N. 2016 On the dispersion of geodesic acoustic modes. *Plasma Phys. Rep*. **42**, 407.

SMOLYAKOV, A.I., NGUYEN, C. & GARBET, X. 2008 Kinetic theory of electromagnetic geodesic acoustic modes. *Plasma Phys. Control. Fusion* **50**, 115008.

SPATSCHEK, K.-H. 2012 *High Temperature Plasmas*. Wiley.

SUGAMA, H. & WATANABE, T.-H. 2006 Collisionless damping of geodesic acoustic modes. *J. Plasma Phys*. **72**, 825.

SUGAMA, H. & WATANABE, T.-H. 2007 Collisionless damping of geodesic acoustic modes. *J. Plasma Phys*. **74**, 139.

WINSOR, N., JOHNSON, J.L. & DAWSON, J.M. 1968 Geodesic acoustic waves in hydromagnetic systems. *Phys. Fluids* **11**, 2448.

ZAKHAROV, V.E. & OSTROVSKY, L.A. 2009 Modulation instability: the beginning. *Physica* D **238** (5), 540–548.

ZHANG, H.S. & LIN, Z. 2010 Trapped electron damping of geodesic acoustic mode. *Phys. Plasmas* **17**, 072502.

ZONCA, F. & CHEN, L. 2008 Radial structures and nonlinear excitation of geodesic acoustic modes. *Europhys. Lett*. **83**, 35001.

ZONCA, F. & CHEN, L. 2014*a* Theory on excitations of drift alfvén waves by energetic particles. I. Variational formulation. *Phys. Plasmas* **21**, 072120.

ZONCA, F. & CHEN, L. 2014*b* Theory on excitations of drift alfvén waves by energetic particles. II. The general fishbone-like dispersion relation. *Phys. Plasmas* **21**, 072121.

ZONCA, F., CHEN, L., BRIGUGLIO, S., FOGACCIA, G., MILOVANOV, A.V., QIU, Z., VLAD, G. & WANG, X. 2015 Energetic particles and multi-scale dynamics in fusion plasmas. *Plasma Phys. Control. Fusion* **57**, 014024.